

# The effect of acquisition resolution on orientation decoding from V1 BOLD fMRI at 7 Tesla

Ayan Sengupta<sup>a,\*</sup>, Renat Yakupov<sup>b</sup>, Oliver Speck<sup>b,c,d,e</sup>, Stefan Pollmann<sup>a,c</sup>,  
Michael Hanke<sup>c,f</sup>

<sup>a</sup>*Department of Experimental Psychology, Institute of Psychology II, Otto-von-Guericke University, Universitätsplatz 2, 39016 Magdeburg, Germany*

<sup>b</sup>*Department of Biomedical Magnetic Resonance, Institute for Experimental Physics, Otto-von-Guericke University, Leipziger Str. 44, 39120 Magdeburg, Germany*

<sup>c</sup>*Center for Behavioral Brain Sciences, Universitätsplatz 2, 39016 Magdeburg, Germany*

<sup>d</sup>*Leibniz Institute for Neurobiology, Brenneckestr. 6, 39118 Magdeburg, Germany*

<sup>e</sup>*German Center for Neurodegenerative Disease (DZNE), site Magdeburg, Leipziger Straße 44, Germany*

<sup>f</sup>*Psychoinformatics lab, Institute of Psychology II, Otto-von-Guericke University, Universitätsplatz 2, 39016 Magdeburg, Germany*

---

## Abstract

A decade after it was shown that the orientation of visual grating stimuli can be decoded from human visual cortex activity by means of multivariate pattern classification of BOLD fMRI data, numerous studies have investigated which aspects of neuronal activity are reflected in BOLD response patterns and are accessible for decoding. However, it remains inconclusive what the effect of acquisition resolution on BOLD fMRI decoding analyses is. The present study is the first to provide empirical ultra high-field fMRI data recorded at four spatial resolutions (0.8 mm, 1.4 mm, 2 mm, and 3 mm isotropic voxel size) on this topic — in order to test hypotheses on the strength and spatial scale of orientation discriminating signals. We present detailed analysis, in line with predictions from previous simulation studies, about how the performance of orientation decoding varies with different acquisition resolutions. Moreover, we also examine different spatial filtering procedures and its effects on orientation decoding. Here we show that higher-resolution scans with subsequent down-sampling or low-pass filtering yield no benefit over scans natively recorded in the corresponding lower resolution regarding decoding accuracy. The orientation-related signal in the BOLD fMRI data is spatially broadband in nature, includes both high spatial frequency components, as well as large-scale biases previously proposed in the literature. Moreover, we found above chance-level contribution from large draining veins to orientation decoding. Acquired raw data were publicly released to facilitate further investigation.

*Keywords:* functional magnetic resonance imaging, acquisition resolution, decoding

---

\*Corresponding author

*Email address:* [ayan.sengupta@ovgu.de](mailto:ayan.sengupta@ovgu.de) (Ayan Sengupta)

## 1 Introduction

2 The term multivariate pattern (MVP) analysis summarizes a range of data analysis  
3 strategies that are highly suitable for studying neural representations encoded in dis-  
4 tributed patterns of brain activity (see, for example, Haxby, 2012; Haynes, 2009; Zhang  
5 et al., 2015; Bonte et al., 2014). While there is an ever increasing number of publications  
6 that demonstrate the power of MVP analysis for functional magnetic resonance imaging  
7 (fMRI) data (Op de Beeck, 2010; Freeman et al., 2011; Alink et al., 2013; Freeman et al.,  
8 2013) with standard resolution (a voxel size of about 2-3 mm isotropic), MVP analysis  
9 is especially promising in the context of high-resolution fMRI. Ongoing technological  
10 improvements, such as ultra high-field MRI scanners (7 Tesla or higher) have pushed  
11 the resolution for fMRI to a level that is approaching the spatial scale of the columnar  
12 organization of the brain (Yacoub et al., 2008; Heidemann et al., 2012). Being able to  
13 use fMRI to sample brain activity patterns at a near-columnar level makes it feasible  
14 to employ MVP analysis with the aim to decode distributed neural representations of  
15 an entire cortical field at a level of detail that is presently only accessible to invasive  
16 recording techniques with limited spatial coverage. However, at this point, it is un-  
17 clear which spatial resolution is most suitable for decoding neural representation from  
18 fMRI data with MVP analysis. While higher resolutions can improve the fidelity of the  
19 BOLD signal by, for example, reducing the partial volume effect (Weibull et al., 2008),  
20 the benefits can be counteracted by physiological noise (such as inevitable motion) and  
21 lower temporal signal-to-noise ratio (tSNR). This raises the question: does the decoding  
22 of neural representations continuously improve with increasing spatial resolution, or is  
23 there an optimal resolution for a given type of representation?

24 In this study, we aim to address this question for the most frequently employed  
25 MVP analysis technique: a cross-validated classification analysis, where a classifier  
26 is repeatedly trained to distinguish patterns of brain activation from fMRI data of a  
27 set of stimulus conditions, and its prediction accuracy is evaluated against a left-out  
28 data portion (Pereira et al., 2009). We selected oriented visual gratings in primary  
29 visual cortex as decoding subject, because it is likely to be the most extensively studied  
30 paradigm regarding the application of MVP analysis on fMRI data, starting with the  
31 classic studies of Kamitani and Tong (2005) and Haynes and Rees (2005). It was  
32 shown that orientation can be decoded reliably at resolutions ranging from standard  
33 3 mm isotropic voxels in the aforementioned studies, to 1 mm (Swisher et al., 2010), and  
34 that it is possible to directly measure orientation columns in V1 with 7 Tesla fMRI of  
35  $0.5 \times 0.5$  mm (in-plane) resolution (Yacoub et al., 2008; Uğurbil, 2012). These findings  
36 led to a discussion on the origin and the spatial scale of the signals that classifiers can  
37 use to learn to discriminate different orientations (*e.g.*, Op de Beeck, 2010; Swisher  
38 et al., 2010; Alink et al., 2013; Freeman et al., 2013). To investigate these questions,  
39 the authors typically acquired high-resolution fMRI and simulated a lower-resolution  
40 acquisition by applying spatial filters to the original data (see Swisher et al., 2010), or  
41 reconstruction of k-space data to different resolutions (Gardumi et al., 2016), in order  
42 to compare metrics, such as prediction accuracy, across a range of spatial frequencies.  
43 However, these approaches have not gone unchallenged as it is unclear to what degree  
44 particular filtering strategies (*e.g.*, Gaussian filtering vs. low-pass filtering in the spatial  
45 frequency domain, see Misaki et al., 2013) can effectively simulate the properties of

46 fMRI recorded at a lower physical resolution, where a change in slice thickness alone  
47 can significantly alter image contrast. Despite this criticism, we are not aware of any  
48 study that has compared the performance of orientation decoding in visual cortex across  
49 a range of physical acquisition resolutions.

50 In this study, we provide empirical data on the effect of spatial acquisition resolution  
51 on the decoding of visual orientation from high field (7 Tesla) fMRI. We recorded BOLD  
52 fMRI data at 0.8 mm, 1.4 mm, 2 mm and 3 mm voxel size while participants were vi-  
53 sually stimulated with oriented phase-flickering gratings using a uniform event-related  
54 paradigm. Chaimow et al. (2011) investigated the effect of acquisition resolution on  
55 decoding of the stimulated eye using simulated 3 Tesla fMRI data based on a model  
56 of ocular dominance columns. They found that a resolution of 3 mm was optimal for  
57 decoding and performance decreased with higher or lower resolution. It is known that  
58 the organization of orientation columns is characterized by higher spatial frequencies  
59 than ocular dominance columns (Obermayer and Blasdel, 1993) and the BOLD point-  
60 spread function (PSF) is considerably smaller than that at 3 Tesla ( $\approx 2.3$  mm FWHM  
61 vs.  $\approx 3.5$  mm FWHM Shmuel et al., 2007; Engel et al., 1997). Considering that, we ex-  
62 pect the maximum orientation decoding accuracy to be observed at a resolution higher  
63 than 3 mm

64 The primary purpose of this study is to explore how spatial resolution as an ac-  
65 quisition parameter, or as a preprocessing outcome impacts decoding. These multi-  
66 resolution data allow for evaluating filtering strategies used in previous studies in terms  
67 of their validity regarding the simulation of lower-resolution fMRI acquisitions from  
68 high-resolution data. These data also enable the investigation of the contributions  
69 of discriminating signal from individual spatial frequency bands for each resolution.  
70 Moreover, we collected high-resolution susceptibility weighted imaging data for blood-  
71 vessel localization in order to investigate the role of large draining veins that may  
72 carry orientation-discriminating signals reflected in low spatial frequency components  
73 when sampled by millimeter range voxels (Kamitani and Tong, 2005; Kriegeskorte and  
74 Bandettini, 2007; Shmuel et al., 2010; Gardner, 2010). In combination with the multi-  
75 resolution fMRI data, we can investigate the effect of this potential signal source on the  
76 orientation decoding at a range of of spatial scales.

77 While our primary focus is on the technical aspect of acquisition resolution for  
78 decoding information from BOLD signal patterns using the representation of visual  
79 orientations as a well-researched example, we acknowledge that these data can be used  
80 to investigate a number of additional questions, such as the specific nature of the en-  
81 coding of visual orientation in the BOLD signal pattern. It can also be a valuable  
82 resource in further optimization of the decoding procedure (classification algorithm,  
83 hyper-parameter optimization, etc.). In order to facilitate the required future anal-  
84 yses we have publicly released the data. It has been uploaded to OpenfMRI (ac-  
85 cession number: ds000113c) and is also available without restrictions from GitHub  
86 <https://github.com/psychoinformatics-de/studyforrest-data-multires7t> and  
87 a description is available in DATA IN BRIEF CITATION. We are hoping that this  
88 dataset and manuscript serve as starting point to a series of additional analysis that  
89 explore aspects beyond acquisition resolution.

## 90 **Materials and methods**

### 91 *Participants*

92 Seven healthy right-handed volunteers (age 21-38 years, 5 males) with normal or cor-  
93 rected to normal vision were paid for their participation. Before every scanning session,  
94 they were provided with instructions for the experiment and signed an informed con-  
95 sent form. The study was approved by the Ethics Committee of the Otto-von-Guericke  
96 University.

### 97 *Stimuli*

98 Following Swisher et al. (2010), a stimulus comprised two semi-annular patches of flick-  
99 ering sine-wave gratings left and right of a central fixation point on a medium gray  
100 background (0.8°-7.6° eccentricity, 160° width on each side with a 20° gap along the  
101 vertical meridian, above and below the fixation point, to aid separation of gratings be-  
102 tween hemifields). Gratings on each side of the stimulus were independently oriented at  
103 either 0°, 45°, 90°, or 135°, with a constant spatial frequency of 1.4 cycles per degree of  
104 visual angle corresponding to the center of the screen, a contrast of 100%, and a flick-  
105 ering frequency of 4 Hz with 50% duty cycle. The phase of the gratings was changed  
106 at a frequency of 4 Hz and was chosen randomly from 0,  $\frac{\pi}{2}$ ,  $\pi$ , or  $\frac{3\pi}{2}$  degrees of phase  
107 angle (Figure 1).

108 Stimulus presentation and response logging were implemented using PsychoPy (v1.79;  
109 Peirce, 2008) running on a computer with the (Neuro)Debian operating system (Halchenko  
110 and Hanke, 2012). Stimuli were displayed on a rear-projection screen (1280×1024 pix-  
111 els resolution; 60 Hz video refresh rate; 25.5 cm wide) located behind the head coil.  
112 Participants viewed the screen via a mirror placed at a distance of  $\approx 4$  cm from their  
113 eyes. The total viewing distance was 100 cm.

### 114 *Behavioral task*

115 In order to keep the participants' attention focused and to minimize eye-movements,  
116 they performed a reading task that was unrelated to the stimulation with oriented  
117 gratings. A black circle (radius 0.25°) was presented as a fixation point at the center  
118 of the screen. Within this circle, a randomly selected excerpt of song lyrics was shown  
119 as a stream of single letters (0.3° height, letter frequency 2 Hz) throughout the entire  
120 length of a run. Each trial started with 3 s of stimulation with oriented gratings and  
121 continued for another 5 s of a task-only period (Figure 1). During task-only periods, a  
122 medium gray background was displayed in both hemifields. At the end of each run, the  
123 participant was asked a question related to the previously read text.

124 In a pilot experiment with in-scanner eye-movement recordings, the letter read-  
125 ing task was found to minimize eye-movements effectively; however, it was unsuitable  
126 to verify fixation accuracy on a trial-by-trial basis. In order to evaluate a potential  
127 impact of the reading task on the orientation decoding performance, the task was re-  
128 placed for one participant with a visual detection task. One participant was repeatedly  
129 presented with a Landolt C stimulus (radius 0.12°, left or right opening (0.048°) at  
130 random intervals in each run. The participants had to respond to the direction of the  
131 opening of the probe by pressing one of two buttons corresponding to a left or right

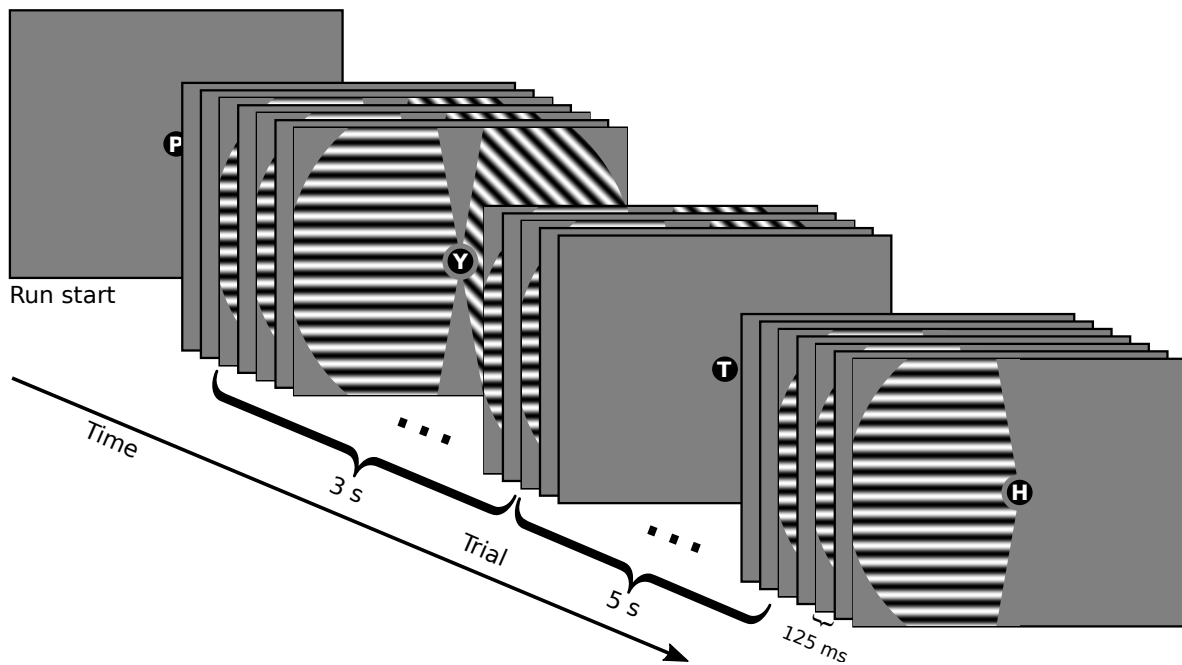


Figure 1: Stimulation paradigm. Independently oriented flickering grating stimuli on a medium gray background were presented in both hemifields for 3 s at the beginning of each trial. Stimulation was followed by a 5 s inter-trial interval. Throughout an entire experiment run, participants performed a continuous central letter reading task to maintain fixation. Interspersed trials where the previous stimulus was repeated in only one of the hemifields were used to decouple stimulation sequences.

132 opening. Discrimination accuracy for this participant was 98.6%, while orientation de-  
133 coding performance did not qualitatively differ from mean decoding accuracy of other  
134 participants. The performance of the subject with the Landolt C task was compared  
135 relative to the 95% binomial proportion confidence interval computed from the number  
136 of correct predictions (BOLD pattern classification), concatenated across hemispheres  
137 and cross-validation fold, and all subjects performing the reading task. For all reso-  
138 lutions (except 3 mm data) the performance of the subject performing the Landolt C  
139 task was within the confidence interval (for 3 mm the decoding accuracy was close to,  
140 but higher, than the upper boundary of the confidence interval). This suggests that  
141 the employed reading task was generally effective in keeping participants focused on  
142 the fixation point.

#### 143 *Procedures*

144 Participants were scanned in five different sessions, one experiment session for each of  
145 the four acquisition resolutions (0.8 mm, 1.4 mm, 2.0 mm and 3.0 mm isotropic) and  
146 one session for retinotopic mapping. These sessions took place on different days over  
147 the course of five weeks. The order of acquisition resolutions was randomized for each  
148 participant. In every experiment session, participants completed ten runs with short  
149 breaks in-between, without leaving the scanner. Each run comprised 30 trials (8 s dura-  
150 tion; 4 min total run duration). In 20 of these trials, a combination of oriented gratings,  
151 one in each hemifield, was presented simultaneously so that each of the four orienta-  
152 tions occurred exactly five times in each hemifield. The sequence of orientations was

153 independently randomized for each hemifield, resulting in random pairings of orienta-  
154 tions within trials. In order to decouple stimulation sequences between hemifields, ten  
155 NULL events were inserted into the trial sequence at pseudo-random positions (a run  
156 could not start with a NULL event and no two NULL events could occur in immediate  
157 succession). NULL events were identical to regular trials, except for the fact that in  
158 one hemifield the same oriented grating as in the previous trial was repeated while the  
159 other hemifield remained empty. The side of the blank hemifield was chosen at random  
160 for each NULL event. For all participants, the actual generated trial sequences show a  
161 roughly equal count of NULL events for each hemifield and frequency of unique com-  
162 binations of grating orientations (refer to supplementary material section *Experimental*  
163 *Design* for more details).

#### 164 *Functional imaging*

165 The objective for functional data acquisition was to obtain BOLD fMRI data from  
166 the V1 ROI at four different resolutions with an identical stimulation paradigm. MR  
167 acquisition parameters were chosen to be maximally similar across resolutions given  
168 two a priori constraints: 1) sufficient spatial coverage of the V1 ROI and 2) identical  
169 sampling frequency (TR) across resolutions.

170 T2\*-weighted echo planar images (EPI) (TR/TE=2000/22 ms, FA=90°) of the oc-  
171 cipital lobe were acquired during visual stimulation using a 7 Tesla whole body scanner  
172 (Siemens, Erlangen, Germany) and a 32 receive channel head coil (Nova Medical, Wilm-  
173 ington, MA). Slices, oriented parallel to the calcarine sulcus (on a tilted axial plane),  
174 were acquired for 4 different spatial resolutions: 3 mm isotropic (FoV=198 mm, matrix  
175 size 66×66, 37 slices, GRAPPA accel. factor 2), 2 mm isotropic (FoV=200 mm, matrix  
176 size 100×100, 37 slices, GRAPPA accel. factor 3), 1.4 mm isotropic (FoV=196 mm, ma-  
177 trix size 140×140, 32 slices, GRAPPA accel. factor 3) and 0.8 mm isotropic (FoV=128×166.4 mm  
178 (AP×LR), matrix size 160×208, 32 slices, GRAPPA accel. factor 4). All EPI scans im-  
179 plemented ascending slice acquisition order and used a 10% inter-slice gap to minimize  
180 cross-slice excitation. For example, for a 3 mm acquisition, the acquired voxel dimension  
181 was 3×3×3 mm, plus a 0.3 mm interslice gap. The sequence for 0.8 mm resolution used  
182 a left-right phase encoding direction in order to avoid wrap-around artifacts, while all  
183 other sequences used anterior-posterior phase encoding. 121 volumes were acquired for  
184 each experiment run and 10 separate scans (one for each experimental run) were per-  
185 formed for each subject. An automatic positioning system (Siemens AutoAlign Head  
186 LS) was used to aid positioning of the field-of-view to the same volume in each scan for  
187 each subject similar to the procedure described in Dou et al. (2014). Online distortion  
188 correction (In and Speck, 2012) was applied to data from all the scans.

189 As a result of the technical constraints the scan volume of the 0.8 mm acquisitions  
190 was substantially smaller than that of the other resolutions and did not cover all of the  
191 V1 ROI. In order to aid co-registration of the small scan volume with the structural  
192 image, an additional EPI acquisition was performed that used the same auto-alignment  
193 procedure, but with a 250×250 in-plane matrix and 57 slices (4s TR). This setup  
194 increased the FoV in the axial plane to cover the full extent of the brain, while the  
195 20 additional slices further increased the coverage along the inferior-superior direction.  
196 60 volumes were acquired to improve image signal-to-noise ratio (SNR) by averaging  
197 across volumes. The resulting volume was used as an intermediate alignment target.

198 Figure S7 illustrates the effect of distortion correction and the alignment quality of  
199 BOLD images to the respective structural images for two participants.

### 200 *Structural imaging*

201 Structural images and susceptibility weighted images were acquired for all participants  
202 in a 3 Tesla Philips Achieva equipped with a 32 channel head coil using standard clin-  
203 ical acquisition protocols. T1-weighted image consisted of 274 sagittal slices (FoV  
204  $191.8 \times 256 \times 256$  mm) and an acquisition voxel size of 0.7 mm with a  $384 \times 384$  in-plane  
205 reconstruction matrix (0.67 mm isotropic resolution). It was recorded using a 3D turbo  
206 field echo (TFE) sequence (TR 2500 ms, inversion time (TI) 900 ms, flip angle  $8^\circ$ , echo  
207 time (TE) 5.7 ms, bandwidth 144.4 Hz/px, SENSE reduction AP 1.2, RL 2.0). A 3D  
208 turbo spin-echo (TSE) sequence (TR 2500 ms, TE eff 230 ms, strong SPIR fat suppres-  
209 sion, TSE factor 105, bandwidth 744.8 Hz/px, SENSE reduction AP 2.0, RL 2.0, scan  
210 duration 7:40 min) was used to acquire a T2-weighted image whose geometric prop-  
211 erties otherwise match the T1-weighted image. A susceptibility weighted image with  
212 500 axial slices (thickness 0.35 mm, FoV  $181 \times 202 \times 175$  mm) and an in-plane acquisition  
213 voxel size of 0.7 mm reconstructed at 0.43 mm ( $512 \times 512$  matrix) was recorded using a  
214 3D Presto fast field echo (FFE) sequence (TR 19 ms, TE shifted 26 ms, flip angle  $10^\circ$ ,  
215 bandwidth 217.2 Hz/px, NSA 2, SENSE reduction AP 2.5, FH 2.0). All the acquisition  
216 protocols used for recording anatomical images and susceptibility images were identical  
217 to those used in Hanke et al. (2014).

### 218 *Region of interest localization*

219 Standard retinotopic measurements were performed using four runs of stimulation with  
220 flickering checkerboard patterns (Warnking et al., 2002), one run each for contract-  
221 ing/expanding rings and clockwise/counter-clockwise wedges. During stimulation, par-  
222 ticipants fixated the center of the screen while performing the letter reading task de-  
223 scribed above. Each run comprised five stimulus cycles, plus 4 s and 12 s of task-only  
224 periods (no checkerboard stimulus) at the start and at the end of a run respectively.  
225 fMRI acquisition took place in the same 3 Tesla scanner as the structural imaging.  
226 Full brain acquisition was performed with T2\*-weighted gradient echo, single-shot echo  
227 planar imaging (EPI) sequence (TR/TE=2000/30 ms, FA= $90^\circ$ , SENSE reduction AP  
228 2) with 3 mm isotropic voxel size, and 10% inter-slice gap (FoV=240 mm, matrix size  
229  $80 \times 80$ , 35 slices, ascending order, anterior-to-posterior phase encoding direction). 90  
230 volumes were acquired in each run.

231 Retinotopic phase maps (polar angle and eccentricity) were generated using the  
232 3DRetinophase tool in the AFNI software package (Cox, 1996). The V1 region was man-  
233 ually delineated on the cortical surface (following the procedure described in Warnk-  
234 ing et al., 2002). Surface reconstruction was performed using the default Freesurfer  
235 `recon-all` pipeline (Dale et al., 1999), using T1 and T2-weighted images as input. V1  
236 delineations on the surface were projected back into a subject’s individual volumetric  
237 space to generate a participant specific V1 ROI mask for the classification analyses.  
238 Figure S7 demonstrates the alignment of the 7T BOLD fMRI with the reconstructed  
239 cortical surface.

240 The associated raw data are available is part of dataset ds000113d on OpenfMRI  
241 and are further described in Sengupta et al. (2016).

242 *Blood vessel localization*

243 A volumetric mask of V1 voxels with venous contributions was generated for each  
244 subject using the following procedure. First, the phase component of the SWI scan was  
245 masked (using a brain mask derived from the magnitude component), and 3D phase  
246 unwrapped with PRELUDE (default settings; Jenkinson, 2003) from FSL (v5.0.8;  
247 Smith et al., 2004). Following the procedure outlined in Haacke et al. (2004), the  
248 unwrapped phase image was spatially high-pass filtered using a mean 'box' filter kernel  
249 (65x65x65 voxels, as implemented in fslmaths; Smith et al., 2004). The high pass  
250 filtered phase component  $\varphi(x)$  was then transformed to a score  $g(x)$  (value interval  
251  $[0, 1]$ ) using  $g(x) = (\pi - \varphi(x))/\pi$  for  $0 < \varphi(x) \leq \pi$  and 1 otherwise. These scores were  
252 multiplied 4 times with the original magnitude image, as suggested by Haacke et al.  
253 (2004), in order to enhance the contrast between venous and non-venous voxels. Blood  
254 vessel masks computed from the thresholded enhanced magnitude image were resliced  
255 into different acquisition resolutions using trilinear interpolation and were constrained  
256 to individual V1 masks for each participant.

257 Separate MVP analyses were performed inside and outside the venous voxels (with  
258 variable mask intensity threshold) in V1 to investigate their individual contributions at  
259 different acquisition resolutions across different threshold levels.

260 The associated raw data are available as part of dataset ds000113 on OpenfMRI  
261 and are further described in Hanke et al. (2014).

262 *Orientation decoding analysis*

263 MVP analysis for orientation decoding was performed with PyMVPA (v2.4.1; Hanke  
264 et al., 2009) on a compute cluster running (Neuro)Debian (v8.0; Halchenko and Hanke,  
265 2012). For feature extraction, BOLD fMRI time series from an individual experimental  
266 run were voxel-wise fitted to hemodynamic response (HR) regressors (boxcar function  
267 convolved with the canonical Glover HRF kernel (Glover, 1999) for each experimental  
268 condition using a general linear model (GLM). Additionally, the GLM design matrix in-  
269 cluded temporal derivatives of HR regressors, six nuisance regressors for motion (trans-  
270 lation and rotation), and polynomial regressors (up to 2nd-order) modeling temporal  
271 signal drift as regressors of no-interest. GLM  $\beta$  weights were computed using the GLM  
272 implementation in NiPy (v0.3; Millman and Brett, 2007) while accounting for serial  
273 correlation with an autoregressive term (AR1). Lastly, separately for every run  $\beta$  scores  
274 were  $Z$ -scored per voxel. The resulting dataset for MVP analysis contained 40 samples  
275 (one normalized  $\beta$  score per condition per run) for each participant.

276 Linear support vector machines (SVM; PyMVPA's `LinearCSVMC` implementation of  
277 the LIBSVM classification algorithm; Chang and Lin, 2011) were used to perform a  
278 within-subject leave-one-run-out cross-validation of 4-way multi-class orientation clas-  
279 sification. This method was selected based on its prevalence in the literature, not  
280 because of an assumed optimal performance in this context. This linear SVM algo-  
281 rithm has one critical hyper-parameter  $C$  that indicates the trade-off between width  
282 of the margin of the classifying hyperplane and number of correctly classified training  
283 data points. While it seems uncommon for neuroimaging studies to optimize this pa-  
284 rameter for a particular application, we observed substantial variability in performance  
285 with varying number of input features. Consequently, we decided to tune this param-  
286 eter using a nested cross-validation approach, where the training portion within each

287 cross-validation fold was subjected to a series of leave-another-run-out cross-validation  
288 analyses in order to perform a grid search for the optimal  $C$  value (search interval  $[10^{-5}$ ,  
289  $5 \times 10^{-2}]$  in 200 equal steps). The “optimal”  $C$  value was then used to train a classifier  
290 on the full training dataset, which was subsequently evaluated on the data from the  
291 left out run. Reported accuracies always refer to the performance on the test dataset  
292 using the tuned  $C$  setting. Tuning of the  $C$  parameter was performed independently  
293 for each participant, resolution, and hemisphere. The ranges of tuned  $C$  parameters for  
294 all resolutions are illustrated in Figure S6.

### 295 *Spatial filtering strategies*

296 In order to investigate how signal for orientation decoding is distributed across the  
297 spatial frequency spectrum, two different strategies for volumetric spatial filtering of  
298 the functional imaging data were implemented.

299 *Gaussian smoothing.* Similar to Swisher et al. (2010), we used Gaussian filtering prior  
300 feature extraction for MVP analysis to estimate the spatial scale of the orientation  
301 specific signal. In the following, the size of the Gaussian filter kernel is described by its  
302 full width at half maximum (FWHM) in mm. Individual filters were implemented using  
303 the following procedure: *Low-pass* (LP) 3D Gaussian spatial filtering was performed  
304 with the `image_smooth()` function in the `nilearn` package (Pedregosa et al., 2011). *High-*  
305 *pass* (HP) filtered images for a particular filter size were computed by subtracting the  
306 respective LP filtered image from the original, unfiltered image. *Bandpass* (BP) filtering  
307 was implemented by a Difference-of-Gaussians (DoG) filter (Alink et al., 2013). Filtered  
308 images were computed by subtracting the LP filtered images for two filter sizes from  
309 each other. For example, an image for the “4-5 mm” band was computed by subtracting  
310 the 5 mm LP filtered image from the 4 mm LP filtered image. It is important to note  
311 that, due to the nature of the filter, the pass-band of a DoG filter is not as narrow  
312 as the filter-size label might suggest. Figure S5 illustrates the attenuation profile of  
313 an exemplary 4-5 mm DoG filter. However, for compactness and compatibility with  
314 previous studies (*e.g.*, Alink et al., 2013) we are characterizing DoG BP filters by the  
315 FWHM size of the underlying LP filters. The respective *band-stop* (BS) filtered image  
316 were computed by subtracting the corresponding BP filtered image from the original,  
317 unfiltered image.

318 Because of its prevalence in standard fMRI analysis pipelines, spatial filtering was  
319 always applied to the whole volume, prior to any masking. However, as this procedure  
320 leads to leakage of information from outside the ROI into the ROI due to smoothing,  
321 particularly with large-sized LP filters, we also performed a supplementary analysis  
322 where filtering was restricted to the V1 ROIs in each hemisphere to prevent information  
323 propagation by smoothing (see supplementary material).

324 *Spatial resampling to other resolutions, with and without Gaussian filtering.* A fre-  
325 quently expressed concern in the literature with respect to Gaussian smoothing is that  
326 a linear transformation does not actually remove high spatial frequency information  
327 (Alink et al., 2013; Kamitani and Sawahata, 2010); instead, it merely implements a  
328 relative scaling of frequency components (see Misaki et al., 2013). In order to explore  
329 any potential impact of an irreversible frequency-domain transformation, we performed

Resolution	V1 Region of Interest				Venous voxels in V1 for two thresholds			
	Left hemisphere		Right hemisphere		>60 <sup>th</sup> percentile		>90 <sup>th</sup> percentile	
	#voxels	std	#voxels	std	#voxels	std	#voxels	std
0.8 mm	7312	1912	7683	2556	1148	446	287	111
1.4 mm	2084	626	2169	710	518	186	130	47
2.0 mm	883	273	898	311	231	84	58	21
3.0 mm	324	94	327	104	105	36	26	9

Table 1: V1 ROI size. Average number of voxels for both hemispheres with standard deviation across participants. The four rightmost columns indicate the number of voxels within the ROI that are considered to be intersecting veins for two different thresholds (the 40% of voxels with the highest volume fraction of blood vessels; and the same for the top 10% voxels; see Figure 6 for an illustration).

330 a Fourier (FFT) based spatial frequency resampling, which destructively removes high-  
 331 frequency components, using the `scipy` function `signal.resample()` (Jones et al.,  
 332 2001). For details on the procedure see the supplementary material. The V1 ROI masks  
 333 were linearly interpolated into the resampled space with the `ndimage.interpolation.zoom()`  
 334 function in `scipy`. FFT resampling was also combined with subsequent Gaussian low-  
 335 pass filtering in order to evaluate a suggestion by Freeman et al. (2013) that one way  
 336 of testing the contribution of fine scale signals to orientation decoding is to compare  
 337 high-resolution BOLD fMRI data down-sampled to conventional resolutions, with or  
 338 without first removing high spatial frequency signals. For all spatial resampling analy-  
 339 sis, with or without Gaussian filtering, all voxels in the respective V1 ROI masks were  
 340 considered for multivariate decoding.

## 341 Results

### 342 *Decoding performance on native acquisition resolution*

343 *Effect of acquisition resolution and number of input voxels.* In order to determine the  
 344 effect of acquisition resolution, we performed orientation decoding at all resolutions.  
 345 Figure 2A shows the mean classification accuracy across participants and hemispheres  
 346 as a function of acquisition resolution in the V1 ROI. In the set of tested acquisition  
 347 resolutions, we found the peak classification performance of 40.89% at 2 mm isotropic  
 348 resolution.

349 For the above analysis, all voxels in the respective V1 ROIs were used. As the  
 350 number of voxels in a 0.8 mm V1 mask was substantially higher than those in a 3.0 mm  
 351 V1 mask (Table 1) and the number of input features/voxels can impact the classification  
 352 performance, we repeated the analysis, but held the number of voxels constant across  
 353 participants and resolutions (50, 100, 125, and 150 voxels). Voxel sub-selection was  
 354 done randomly, and the analysis was repeated 100 times with a new random selection  
 355 of voxels. Figure 2B shows that a constant and smaller number of input voxels had  
 356 a negative effect on classification performance. Classification performance was better  
 357 with 2.0 mm and 3.0 mm data as compared to 0.8 mm and 1.4 mm data.

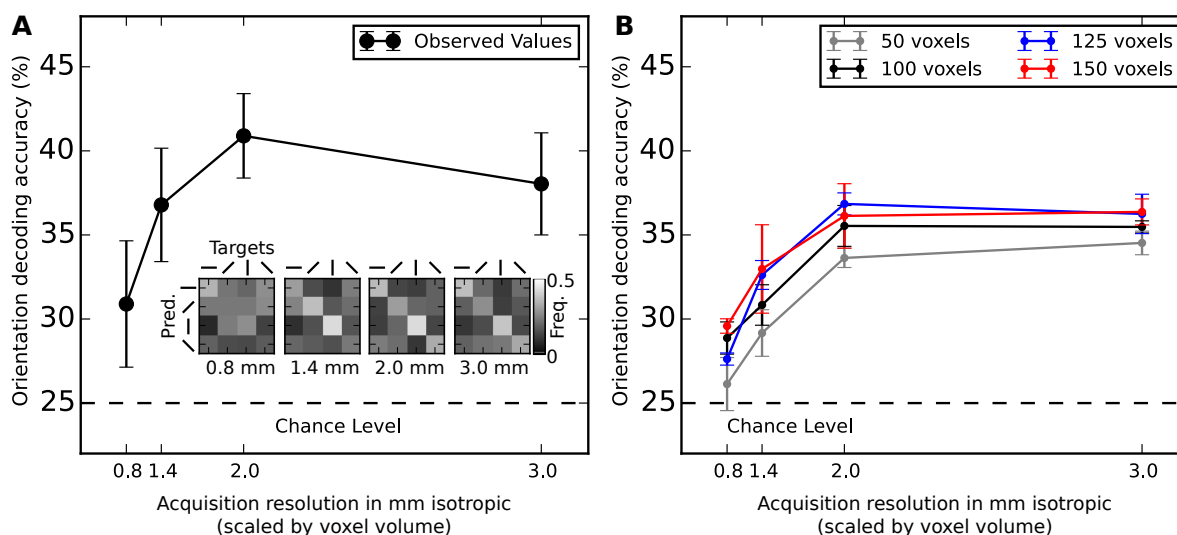


Figure 2: **(A)** Orientation decoding accuracy on spatially unfiltered data as a function of acquisition resolution in the whole contralateral V1 ROI. Error bars show the standard error of the mean (SEM) across 7 participants averaged across hemispheres. Chance level accuracy (25%) is indicated as a horizontal dashed line. Classification performance is detailed in confusion matrices for each resolution depicting the frequency of correct classification for each combination of prediction and target values. **(B)** Analog to **(A)**, but with a constant number of input voxels across resolutions. 50, 100, 125, or 150 voxels were selected at random from the the whole contralateral V1 ROI for the classification analysis. Selection was repeated 100 times. Error bars show SEM across repetitions. Upper range limit of 150 voxels was determined by the ROI with the least number of voxels at 3 mm resolution.

358 *Time-series signal-to-noise ratio (tSNR)*. It has been shown that overall contrast-to-  
 359 noise ratio (OCNR) is a factor that impacts classification performance (Chaimow et al.,  
 360 2011). According to Chaimow et al. (2011) OCNR is proportional to contrast range  
 361 and the square root of the number of voxels and is inversely proportional to the noise  
 362 level. The noise level was calculated as the inverse of time course signal-to-noise ratio,  
 363 which in turn depends on voxel size (Triantafyllou et al., 2005). In this study, tSNR is  
 364 modulated across acquisition resolutions due to differential impact of technical/thermal  
 365 and physiological noise components. In order to characterize this impact, we computed  
 366 tSNR for each voxel as the ratio of mean signal intensity across all time points after  
 367 polynomial detrending (1<sup>st</sup> and 2<sup>nd</sup> order; analog to preprocessing for MVP analysis)  
 368 of scanner drift noise and the corresponding standard deviation. Voxel-wise tSNR was  
 369 averaged across all experiment runs. For a tSNR estimate of the whole ROI, we averaged  
 370 this score across all voxels. The relationship of voxel volume and tSNR in the empirical  
 371 data can be well explained by the following model (Triantafyllou et al., 2005):

$$tSNR = \kappa V / \sqrt{1 + \lambda^2 \kappa^2 V^2}$$

372 where  $V$  is the voxel volume,  $\kappa$  is the proportionality constant, and  $\lambda$  is the magnetic  
 373 field strength independent constant parameter with  $\lambda=0.0117$ ,  $\kappa=22.74$  ( $R^2=0.95$ ) The  
 374 estimated asymptotic tSNR limit of  $\approx 85$  ( $\frac{1}{\lambda}$ ) is similar to the report of Triantafyllou  
 375 et al. (2005) for 7 Tesla acquisitions and is reached around 2.5 mm acquisition resolution  
 376 (see supplementary Figure S8).

377 Figure 3A illustrates the non-linear relation of tSNR and orientation decoding ac-

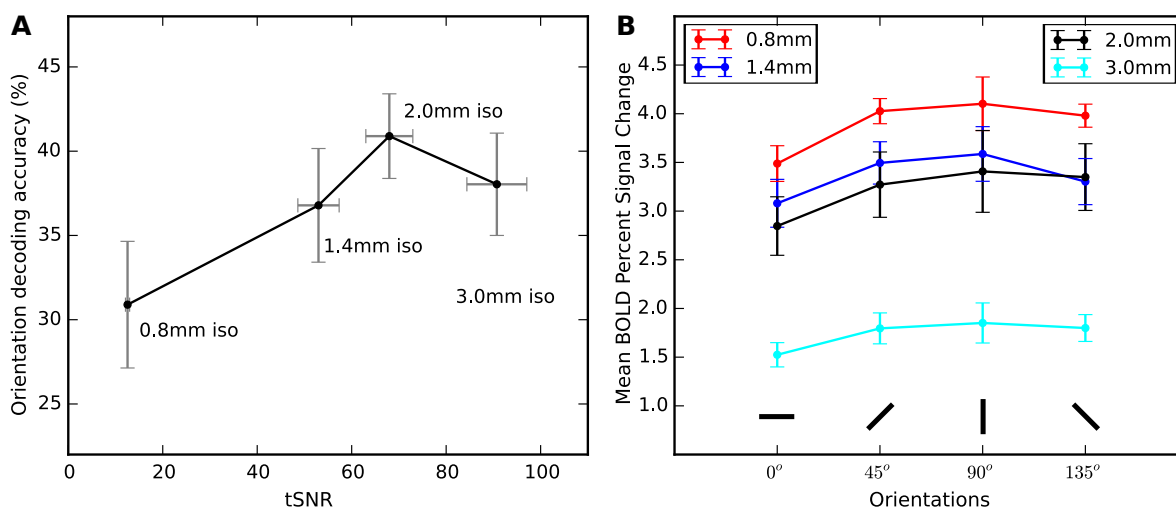


Figure 3: **(A)** Orientation decoding accuracy vs. temporal signal-to-noise ratio (tSNR) for the four measurements (resolutions). Error bars show the SEM for tSNR and accuracy across subjects and hemispheres. **(B)** Estimated BOLD signal change by orientation for all resolutions. Maximum pairwise signal change difference is observed for the cardinal directions 0° and 90°. This pattern is congruent with the confusion plots in Figure 2A.

378 accuracy. We observe a substantial drop in accuracy when decreasing resolution from  
 379 2 mm to 3 mm, despite a further increase in tSNR. This non-linearity was not observed  
 380 by Gardumi et al. (2016), who only reported a positive trend for the correlation be-  
 381 tween decoding accuracy and tSNR, based on a single acquisition (1.1 mm resolution  
 382 with comparable tSNR of  $\approx 32$ , and other resolutions being generated by reconstructing  
 383 k-space data to lower resolutions).

384 *BOLD signal change.* Another potential source of differences in orientation decoding  
 385 accuracy across resolutions are BOLD signal amplitude differences due to, for example,  
 386 differential impact of a partial voluming effect (see Tong et al., 2012; Alink et al., 2013).  
 387 In order to quantify this effect, we calculated mean percentage BOLD signal change  
 388 in response to any flickering orientation stimulus across resolutions using FeatQuery in  
 389 FSL (v5.0.8; Smith et al., 2004). Similar to preprocessing in MVP analysis, no spatial  
 390 smoothing was performed before calculating the percentage signal change. In order to  
 391 obtain comparable percentage signal change across resolutions, we obtained a mask of  
 392 all responsive V1 voxels ( $z > 2.3$  with  $p < 0.05$  default parameters of FSL FEAT)  
 393 in 0.8 mm data for every subjects (Swisher et al., 2010, similar to Figure 3). The  
 394 responsive V1 voxel mask obtained at 0.8 mm was resliced into 1.4 mm, 2.0 mm and  
 395 3.0 mm resolutions. Percentage signal change was calculated with FeatQuery within  
 396 these masks. We found that the mean percentage BOLD signal change was the highest  
 397 for 0.8 mm resolution: 4.51% (0.8 mm), 3.92% (1.4 mm), 3.73% (2.0 mm), and 2.05%  
 398 (3.0 mm).

399 Previous studies found differential BOLD response magnitudes to different visual  
 400 orientations. Furmanski and Engel (2000) reported stronger responses to cardinal  
 401 orientations. In contrast, Swisher et al. (2010) found greater responses to oblique  
 402 orientations. In order to test for a differential effect and a possible interaction be-  
 403 tween orientation and acquisition resolution, we computed a 2-factor (orientation and

404 resolution) within-subject ANOVA for the estimated BOLD signal change from all  
405 7 subjects (Figure 3B). There was a significant main effect of acquisition resolution  
406 ( $F(3, 18) = 32.99, p < 0.001$ ). We found no statistically significant main effect of orien-  
407 tation ( $F(1.22, 7.319) = 4.678, p = 0.061$ ; using Greenhouse-Geisser correction due to  
408 violation of sphericity assumption, Mauchly's test  $p = 0.002$ ). There was a non signifi-  
409 cant interaction between the factors, resolution, and orientation ( $F(2.947, 17.68) = 1.96,$   
410  $p = 0.158$  after Greenhouse-Geisser correction).

411 *Impact of head motion on decoding accuracy.* Head motion is a likely factor to impact  
412 decoding accuracy. In order to evaluate this effect, we calculated a head motion index  
413 suggested by Alink et al. (2013) for every participant and acquisition resolution. Inline  
414 with the findings of Gardumi et al. (2016), we found a consistent, but non-significant  
415 trend towards a negative correlation between head motion and decoding accuracy across  
416 acquisition resolutions 0.8 mm:  $r = -0.45, p = 0.30$ ; 1.4 mm:  $r = -0.64, p = 0.11$ ; 2.0 mm:  $r = -$   
417  $0.68, p = 0.09$ ; 3.0 mm:  $r = -0.23, p = 0.60$ ).

418 *Decoding performance on spatially filtered data*

419 *Impact of Gaussian smoothing.* Figure 4 A-D show the impact of Gaussian filtering  
420 on the classification performance for data from all four acquisition resolutions. LP  
421 spatial filtering is most commonly performed as a noise reduction step in fMRI data  
422 pre-processing. The classification performance achieved on HP filtered data of the same  
423 filter size is an indication of the amount of usable information removed by LP filtering.  
424 Classification performance on BP filtered data indicates whether usable information is  
425 present in a particular band of spatial frequencies. Likewise, band-stop performance  
426 indicates the presence of usable information anywhere, except in a particular band.

427 Except for 0.8 mm and 1.4 mm data, we observed no increase in mean decoding for  
428 LP filtering, compared to performance on unfiltered data. For all resolutions, except for  
429 0.8 mm, we see observe the best performance after LP filtering with kernel sizes no larger  
430 than 3 mm FWHM. Peak performance on HP filtered data was achieved for filter sizes  
431 larger than 9 mm FWHM, except for the 0.8 mm acquisition resolution. We investigated  
432 via BP filtering which frequency bands were most informative for orientation decoding  
433 across all acquisition resolutions, using DoG BP filters with a 1 mm difference in the  
434 FWHM size of the underlying Gaussian filters (Figure 4 A-D; black curves). The results  
435 show peak performance of BP filtering yielded for all acquisition resolutions in the range  
436 of  $\approx 5$ -8 mm (highlighted range).

437 Average decoding accuracy of BS filtered data remained above-chance for all spatial  
438 frequency bands. The BS performance curve initially follows the LP performance for  
439 small filter sizes, but resembles the HP performance for larger filter sizes.

440 *Impact of spatial resampling to other resolutions, with and without Gaussian smooth-*  
441 *ing.* As an alternative approach to Gaussian LP filtering for simulating a resolution  
442 reduction, data acquired in a particular resolution were resampled (FFT-based trans-  
443 formation) to all other resolutions and classification analysis was performed with and  
444 without additional prior Gaussian LP filtering, as suggested by Freeman et al. (2013).  
445 The results are depicted in Figure 5.

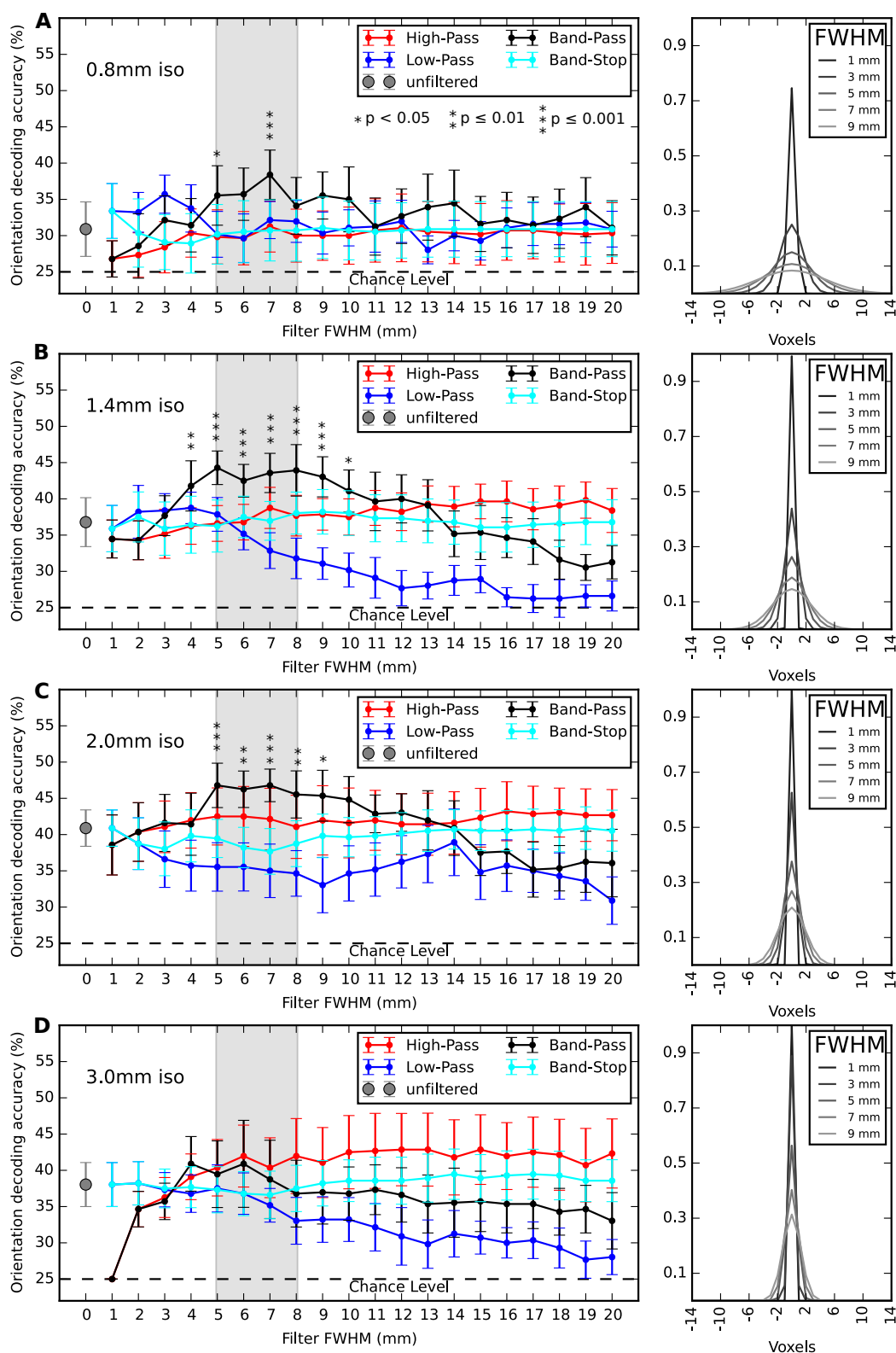


Figure 4: Orientation decoding accuracies for all acquisition resolutions (increasing acquisition voxel size from top to bottom) and levels of spatial high-pass, low-pass, band-pass, and band-stop Gaussian filtering. Panels on the right visualize the size of selected Gaussian filter kernels with respect to the voxel size at each resolution. FWHM values for band-pass and band-stop filters refer to the corresponding 1mm band to the closest smaller filter size (e.g., 5 mm refers to the 4-5 mm band). McNemar test (Edwards, 1948) was used to comparing the performance of the BP filtered data with the unfiltered decoding performance. Star markers indicate a significant difference (Bonferroni-corrected, see legend in (A) for criteria).

446 We observed no general benefit of spatial down-sampling with respect to decoding  
447 accuracy. We also did not see systematically improved accuracies after LP filtering  
448 across resolutions.

449 Data acquired at 2.0 mm or 3.0 mm showed a general trend towards higher decod-  
450 ing accuracy after resampling (up-sampling or down-sampling) compared to the corre-  
451 sponding native acquisition resolution, even with prior Gaussian LP filtering of different  
452 kernel sizes. 0.8 mm data consistently showed low decoding accuracy when resampled  
453 to any other resolution with or without Gaussian filtering.

#### 454 *Vascular contribution to orientation decoding*

455 Orientation decoding again performed inside and outside the vein localizer mask in  
456 the V1 ROI in order to evaluate the availability of orientation discriminating signal in  
457 the vascular system. Two different, arbitrary thresholds were used to classify voxels  
458 as intersecting vs. non-intersecting with veins, based on the co-registered and re-sliced  
459 vein mask: the top 40% and top 10% of voxels with the highest value after realignment  
460 and reslicing to the target resolution with trilinear interpolation. The resulting number  
461 of voxels are presented in Table 1.

462 Analyses outside the vein mask were performed twice: once for the entire region  
463 and again for a subset of voxels that was constrained to the number of voxels inside  
464 the vein mask for the corresponding resolution. In the latter case, the analysis was  
465 repeated with a new random voxel selection 100 times.

466 Figure 6A (right panel) shows that voxels with the highest venous content in their  
467 volume still yield above chance decoding performance. The performance drop for the  
468 two lowest resolutions between the two vein mask thresholds may be explained by the  
469 low number of input features going into the classification at high threshold (compare  
470 Figure 6A, left panel). At 0.8 mm, the 10% most venous voxels yield the same decoding  
471 performance as the rest of the V1 ROI combined (Fig. 6, middle panel), and noticeably  
472 more than a corresponding number of randomly samples non-venous voxels (Fig. 6A,  
473 middle panel). Similar results can be observed for the 1.4 mm resolution.

## 474 **Discussion**

475 In order to explore the effect of acquisition resolution and spatial filtering on the de-  
476 coding of visual orientations from primary visual cortex, we measured ultra-high field  
477 7 Tesla fMRI data at four different resolutions from seven participants. Linear SVM  
478 classifiers were trained to classify voxel patterns of regression weights of hemodynamic  
479 response models for the visual stimulation with four different oriented gratings. Cross-  
480 validated classification accuracy was used as performance metric.

481 The overall classification accuracies reported here are deceptively low (peaking at  
482 40-50% with a theoretical chance-level performance of 25% for the 4-way classification  
483 analyses employed in this study). Other decoding studies in the literature have often  
484 used binary classification paradigms (for example, Alink et al., 2013; Chaimow et al.,  
485 2011) or reported average pairwise accuracy for classification performance results like  
486 (*e.g.*, Kamitani and Tong, 2005; Op de Beeck, 2010). Converted into average pairwise  
487 binary accuracies, the results reported here range from 55% to 70% (for 0.8 mm and  
488 2 mm respectively, each accuracy corresponding to an analysis of the full V1 ROI and

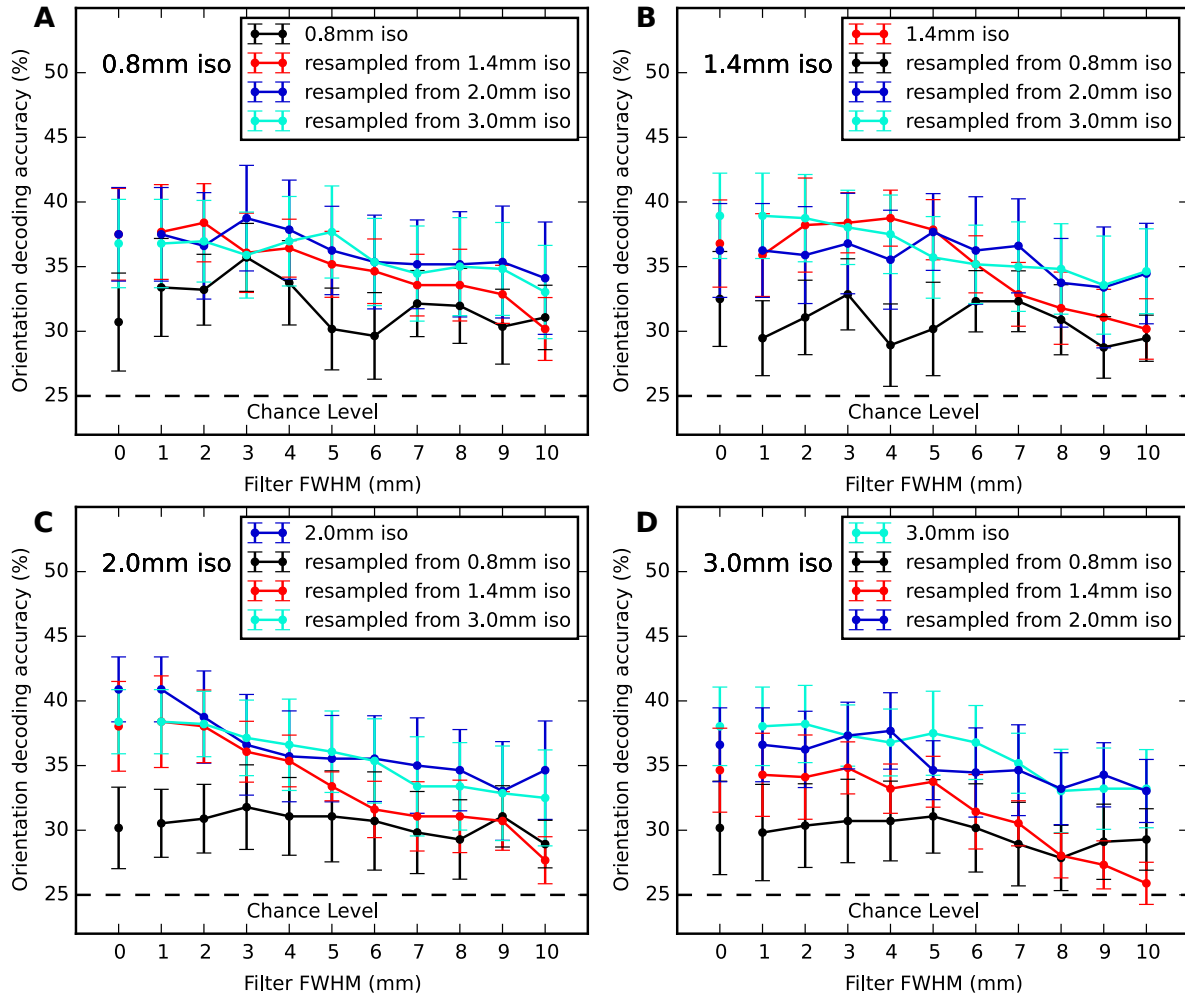


Figure 5: Orientation decoding performance on fMRI data resampled to other spatial resolutions, with and without different levels of prior low-pass Gaussian spatial filtering. Each panel title indicates the respective resolution after spatial resampling. The panel legends identify the corresponding original native acquisition resolutions. The color coding consistently identifies the native resolution across all four panels. The disconnected data points at 0 mm represent the decoding accuracy after spatial resample *without* prior Gaussian LP filtering. Recording high-resolution data with subsequent spatial down-sampling tends to yield lower classification accuracies compared to the native resolution acquisition, with or without prior Gaussian low-pass filtering of any tested kernel size.

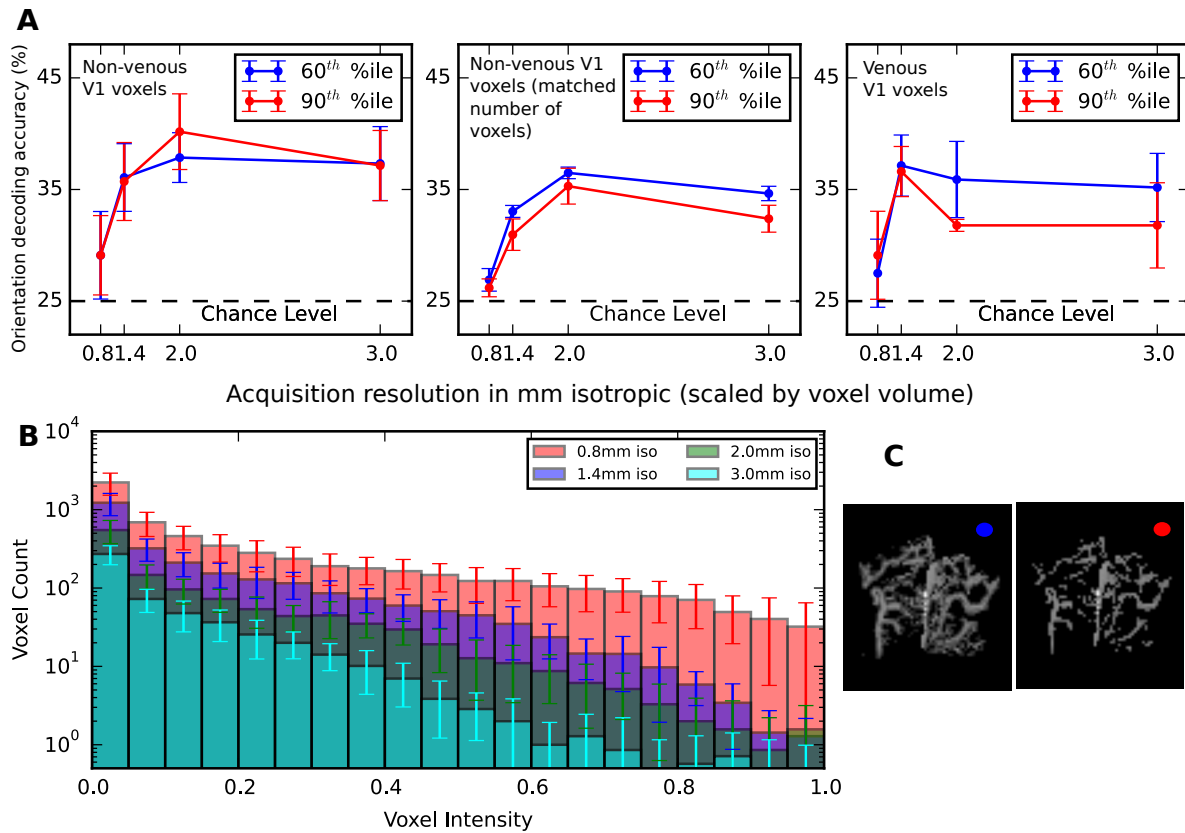


Figure 6: **(A)** Decoding accuracy computed inside and outside the vein mask within the V1 ROI. The vein masks obtained from susceptibility weighted imaging were thresholded at two different levels i.e. 60 percentile and 90 percentile. The panel on the left shows the performance of the entire V1 ROI outside the vein mask (non-venous voxels) for the two different thresholds. Orientation decoding accuracy on V1 voxels restricted to the veins mask (venous voxels) is shown on the right panel. The middle panel depicts the average decoding performance of non-venous voxels that randomly sampled in number to the corresponding venous voxels. The dashed horizontal lines indicate the chance performance. **(B)** Trilinear interpolation was used to reslice the vein mask to all four target resolutions. The histogram shows the distribution of mask voxel intensities corresponding to the volumetric fraction of “vein voxels” in the high-resolution vein mask (voxel count axis in log-scale). **(C)** Axial maximum intensity projection of the vein mask of one participant resliced to the 0.8mm resolution; illustrates the two chosen thresholds. The color indicator correspond to the curves depicted in panel A.

489 with no additional smoothing; see Figure 2A; theoretical chance-performance: 50%),  
490 hence accuracies are of the same magnitude as in other studies (see, for example, Haynes  
491 and Rees, 2005; Alink et al., 2013). In addition, some studies like Swisher et al. (2010)  
492 also reported similar unfiltered accuracy results ( $\approx 50\%$ ) in a 4-way classification anal-  
493 ysis with  $0^\circ$ ,  $45^\circ$ ,  $90^\circ$ , and  $135^\circ$  gratings with much longer stimulation time (a block  
494 design of 18s of block duration and 8 blocks/run). Therefore, we conclude that the  
495 overall quality of the present data is comparable to that of previous studies, and that  
496 the results presented here can be used to address open questions regarding the impact  
497 of data acquisition and spatial filtering parameters on the decoding of orientation from  
498 the early visual cortex. Importantly, in this experiment we did not use a univariate  
499 feature selection approach to define the “visually responsive” voxels in V1 (for exam-  
500 ple a GLM contrast) in an attempt to improve the decoding accuracy. Studying the  
501 potential impact of such an approach is left to a future study.

502 Given the uncertainty of how much a further optimization of the decoding procedure  
503 – *e.g.*, the specific classification algorithm, hyper-parameter optimization strategy, and  
504 feature selection method – would impact the results, we consider the interpretation of  
505 the present results regarding the nature of the signal source as a starting point for a  
506 further exploration of their robustness respect to variations of analysis parameters not  
507 considered here.

#### 508 *Optimal acquisition resolution*

509 Among the four tested acquisition resolutions, the highest decoding accuracy was  
510 observed with a 2 mm resolution (Figure 2A). This result is congruent with a simulation  
511 study by Chaimow et al. (2011) that analyzed the impact of anatomical and physio-  
512 logical properties of primary visual cortex, as well as technical parameters of BOLD  
513 fMRI acquisition on the accuracy of decoding the stimulated hemifield from signal sam-  
514 pled from ocular dominance columns. The aforementioned study included a number  
515 of predictions for choosing optimal voxel size and number of input voxels to maximize  
516 decoding accuracy for 3 Tesla fMRI (see Figure 6 in Chaimow et al., 2011) that show a  
517 striking similarity to the results presented here (Figure 2). For 3 Tesla fMRI, Chaimow  
518 et al. (2011) showed that peak decoding accuracy is achieved around 3 mm in-plane  
519 voxel size for ocular dominance. Given that the profile of orientation columns has  
520 higher spatial frequency compared to ocular dominance columns (Obermayer and Blas-  
521 del, 1993) and the BOLD PSF at 7 Tesla is considerably smaller compared to 3 Tesla  
522 (Shmuel et al., 2007; Engel et al., 1997) a higher optimal resolution was to be expected  
523 for this study, and this hypothesis is supported by our results. This finding is also inline  
524 with a recent study by Gardumi et al. (2016) showing that optimal decoding accuracy of  
525 speaker identity, or phonemes, from auditory cortex BOLD patterns could be achieved  
526 with an effective voxel size of 2.2 mm (acquisition resolution was 1.1 mm and target  
527 resolution was achieved by reconstructing k-space data to a lower resolution), although  
528 the nature of the commonality between these findings remains to be investigated.

529 Superior decoding performance at 2 mm was still observed even when the number  
530 of input voxels for classification was held constant across resolutions, although the per-  
531 formance differences between resolutions are reduced (Figure 2B). The ratio of input  
532 features (voxels) and the number of observations (fixed in this study) is a critical factor  
533 for the training of a classification model, as with increasing dimensionality the sampling

534 of the feature space becomes sparser, and, consequently, the estimated decision surface  
535 suffers from increased uncertainty (curse of dimensionality, Bellman, 1961, after Fried-  
536 man et al. 2001) In this study, the number of voxels in the ROI varies by a factor of  
537  $>20$  from the lowest to the highest resolution (Table 1) and the coverage volume also  
538 varies across resolutions. Despite full V1 coverage for the 1.4 mm (except for one sub-  
539 ject), 2 mm, and 3 mm acquisitions, peak decoding accuracy was observed with 2 mm  
540 data. There is no noticeable difference between accuracies for the lowest resolutions  
541 when the number of input voxels is held equal (Figure 2B). The pattern of decoding  
542 accuracy differences when using the full ROI vs. a constant number of voxels across all  
543 resolutions could indicate that  $\approx 700$  input voxels (size of the ROI at 2 mm) represents  
544 the optimal trade-off between the number of observations and input voxels, given the  
545 noise in the data and the fixed number of observations in this study.

546 Moreover, the present data suggest, in line with Chaimow et al. (2011), that tem-  
547 poral signal-to-noise-ratio, an indicator of temporal signal stability, is a critical factor  
548 for optimal decoding accuracy (Figure 3A), whereas the magnitude of BOLD signal  
549 change was not found to be relevant. While the overall BOLD signal change amplitude  
550 at 0.8 mm (4.51%) was higher than that at 2.0 mm (3.73%), the decoding performance  
551 was superior for 2.0 mm data. In fact, 0.8 mm data showed the largest magnitude of  
552 BOLD signal change but, at the same time, showed the lowest decoding accuracy among  
553 all resolutions.

554 Previous studies have reported BOLD response magnitude differences for different  
555 orientations. Furmanski and Engel (2000) reported that cardinal orientations elicited  
556 higher activation changes than oblique orientations of circular gratings. Swisher et al.  
557 (2010), who used the same kind of hemifield gratings as in the present study, reported  
558 higher activation for oblique than cardinal orientations. The pattern observed in this  
559 study diverges from both previous results showing a tendency for activation to be lowest  
560 for  $0^\circ$  and highest for  $90^\circ$  orientations, with oblique orientations in between. While we do  
561 not find statistically significant evidence for a differential average response magnitude  
562 across orientations at the ROI level, this does not rule out the presence of univariate  
563 orientation-discriminating signal in a subset of the input features/voxels.

564 It has to be noted that the comparison of decoding performance on 0.8 mm data  
565 with other resolutions is compounded by several factors. First and most importantly,  
566 the V1 coverage at this resolution was limited for technical reasons (imposed by the  
567 requirement to keep the TR at a common 2 s interval across all resolutions). This likely  
568 leads to a general underestimation of the performance at this resolution, which affects  
569 both the analyses of the full ROI, as well as those sub-sampling a smaller number  
570 of voxels. Moreover, the small coverage, combined with the impact of any residual  
571 geometric distortions, and the additional intermediate alignment step make accurate  
572 BOLD-to-structural alignment more challenging at 0.8 mm than at any other resolution.  
573 Precise alignment is important, as the V1 ROI is initially defined on the reconstructed  
574 cortical surface. Any suboptimal alignment will therefore impact decoding accuracy at  
575 0.8 mm more than other resolutions. Lastly, the search range for C-value SVM hyper-  
576 parameter was insufficient for 0.8 mm scans, the C-value was predominantly set to the  
577 lower search range boundary (Fig. S6). The search range was determined on a pilot  
578 scan and held constant for all analyses to avoid circularities. A more suitable parameter  
579 optimization scheme could have led to different results.

580 *Optimal low-pass spatial filtering*

581 Gaussian spatial LP filtering is one of the most common preprocessing steps for  
582 fMRI data analyses. However, the present findings indicate that explicit spatial LP  
583 filtering, in addition to the implicit spatial filtering due to inherent motion, and the  
584 effect of head movement correction algorithms is generally not beneficial for orientation  
585 decoding (Figure 4). Only for resolutions higher than 2 mm does additional spatial  
586 smoothing with 2-3 mm FWHM show a tendency for improved decoding accuracy. This  
587 suggests that, given a resolution, a spatial smoothness equivalent to a Gaussian kernel  
588 size of  $\approx 2$  mm FWHM is optimal. This is congruent with the observation of overall  
589 lower decoding accuracies for 3 mm scans and is in line with the prediction of optimal  
590 acquisition resolution between 2 mm and 3 mm as presented above.

591 Moreover, spatial down-sampling is not beneficial for orientation decoding either.  
592 As shown in Figure 5 (0 mm data points, corresponding to no Gaussian smoothing),  
593 orientation decoding on down-sampled data does not outperform the decoding on data  
594 natively recorded in the corresponding resolution (as for example, in the 2.0 mm panel  
595 of Figure 5, the 0.8 mm and 1.4 mm downsampled data performed lower than native  
596 2.0 mm data).

597 *Spatial characteristics of orientation specific signals*

598 The analysis of individual spatial frequency bands via BP filtering (Fig. 4) revealed  
599 that orientation-related signal is present in a wide range of spatial frequencies as in-  
600 dicated by above-chance decoding performance for nearly all tested bands. However,  
601 a drop in decoding accuracy can be observed across all resolutions for bands with a  
602 12 mm FWHM (or larger) Gaussian kernel as the smaller kernel in the LP filter pair  
603 used for BP filtering.

604 Freeman et al. (2013), states that it is still an open question whether fMRI can re-  
605 flect signals originating from sampling random irregularities in the fine-scale columnar  
606 architecture (spatial scale  $\approx 1$  mm). This study also suggests that given a columnar ar-  
607 chitecture in the human visual cortex (Adams et al., 2007), BOLD fMRI measurements  
608 at conventional resolution  $\approx 2$  mm might reflect a combination of fine-scale and coarse-  
609 scale (spatial scale  $\approx 10$  mm) contributions. Similarly, we can interpret the present re-  
610 sults such that the orientation-discriminating signal picked up from these BOLD fMRI  
611 data is spatially broadband in nature, includes both high spatial frequency components,  
612 as well as large-scale biases. On one hand the highest decoding accuracy was observed  
613 at 2 mm resolution, and low pass filtered components generated above chance accuracies  
614 beyond 10 mm FWHM Gaussian smoothing (similar to Op de Beeck, 2010). These ob-  
615 servations point to indicate that low frequency components provide orientation specific  
616 signals. On the other hand we found that for DoG BP filters Gaussian kernel sizes of  
617 4 and 5 mm FWHM and larger, decoding performance on BP filtered data was higher  
618 than the LP filtered components at all acquisition resolutions. This result pattern is an  
619 indication that low spatial frequency fMRI components also contribute to noise with  
620 respect to orientation discrimination.

621 According to Freeman et al. (2013), a test for fine-scale signals ( $\approx 1$  mm, according  
622 to the definition by Freeman et al.) underlying the ability to decode orientations would  
623 be a comparison between decoding accuracies after down-sampling high-resolution mea-  
624 surements to conventional scanning resolutions, with and without prior removal of the

625 columnar-scale contributions. To investigate this topic, we did FFT based resampling  
626 of the BOLD fMRI data from their native resolution into all three alternative reso-  
627 lutions with or without prior removal of low frequency components (Fig. 5). We did  
628 not observe an increase in decoding accuracy after down-sampling data from our two  
629 highest resolutions (0.8 mm and 1.4 mm), regardless of any prior LP Gaussian filtering  
630 (except for a single case of performance increase when resampling 0.8 mm to 1.4 mm  
631 data without prior LP filtering, at a comparatively low overall accuracy level). From  
632 these findings we conclude that the orientation-related signal used for decoding is un-  
633 likely to comprise of low-frequency components alone. This conclusion is in line with  
634 Swisher et al. (2010) who also reported that “majority of orientation information in  
635 high resolution fMRI activity patterns can be found at spatial scales ranging from the  
636 size of individual columns to about a centimeter”.

637 Carlson (2014) identified neuronal activity patterns related to stimulus edges that  
638 mimic a radial bias as a potential source of a global signal bias. The stimuli employed  
639 in this study had clearly visible, unsmoothed edges, hence edge-related activity is a  
640 valid explanation for the observed orientation-related large-scale signals. It can be  
641 argued that the V1 ROI could be adjusted by a “safety margin” to the representation  
642 of the edge of the stimuli to reduce edge related signals. We have tested various criteria  
643 for ROI definition and sizes. We have found very little variation of the results with  
644 respect to the particular shape and size of the ROI. The reported results are based  
645 on a V1 ROI generated by retinotopic mapping that used a stimulus that was larger  
646 than our visual orientation stimulus, hence we have likely sampled voxels representing  
647 edge-related signals. In other words, our ROI should contain a maximum amount of  
648 stimulus-related information present in V1. We leave an analysis exploring aspects of  
649 the relationship of individual stimulus properties and ROI shapes with the BOLD signal  
650 and decoding to a future study.

651 Overall, BP filtering yielded peak performances for all resolutions (except for the  
652 3 mm acquisition). Consistent with Alink et al. (2013), the present results suggest that  
653 a band matching a DoG BP filter consisting of a 5 mm and an 8 mm FWHM Gaus-  
654 sian LP filter) carries most (but not all) orientation-related signal. This band covers  
655 wavelength from about 4.5 mm to 1.6 cm (Fig. S5). The Nyquist-Shannon Sampling  
656 Theorem dictates that, in order to measure a particular signal appropriately, the sam-  
657 pling frequency has to be at least twice the critical frequency of that signal. Hence,  
658 a 3 mm acquisition can only sample frequencies with a wavelengths of 6 mm or larger,  
659 and consequently misses some part of this most informative band.

660 This is consistent with our finding that optimal decoding accuracy required a reso-  
661 lution higher than 3 mm. The nearly identical peak performance on 1.4 mm and 2 mm  
662 data is also compatible with this minimum frequency rule. However, the markedly  
663 lower decoding performance on 0.8 mm could be considered evidence that a minimum  
664 sampling resolution is necessary but not sufficient for optimal decoding performance. In  
665 this study, an optimal balance of scanning resolution and temporal signal-to-noise-ratio  
666 is reached at 2 mm resolution. Higher resolution reduce tSNR and lower resolutions do  
667 not provide sufficient sampling of higher frequency signals.

668 Within the limits of our analyses the presented results do not show evidence for a  
669 variation of informative spatial frequency bands across acquisition resolutions as one  
670 might observe when a high spatial frequency signal of orientation columns in early vi-

671 sual cortex is reflected in (much larger) fMRI voxels by means of spatial aliasing. In  
672 the case of spatial frequency aliasing (Nyquist-Shannon Theorem) the frequency of the  
673 observed, aliased signal would vary depending on the actual sampling frequency (size  
674 of the voxel), due to an insufficient sampling frequency by the voxel grid. Here, the  
675 peak decoding performance (as found after BP filtering) is always located in the same  
676 band across all four resolutions. However, the DoG filters used here to investigate the  
677 importance of particular frequency bands feature a relatively large passband (Fig. S5)  
678 that does not allow to rule out spatial aliasing of orientation-discrimination signal. The  
679 absence of evidence for spatial aliasing is in line with Kamitani and Tong (2005) and  
680 Chaimow et al. (2011) which show that the spatial frequencies of columnar structures  
681 (0.5 cycles/mm) do not contribute signal for decoding, due to several technical limi-  
682 tations like inherent head motion and reduced SNR proportional to reduction in voxel  
683 volume. Moreover, Shmuel et al. (2007) state that the PSF — that captures blurring  
684 factors due to eye movements, neuronal response, BOLD response PSF in gray matter,  
685 as well as the PSF of the data acquisition process — makes fMRI data inherently LP  
686 filtered and, as such, poses a physical limitation on the spatial frequency scale from  
687 which fMRI signal can be obtained. Kamitani and Tong (2005) and Chaimow et al.  
688 (2011) identify contributions from random variations and irregularities in the columnar  
689 structures captured by larger voxels as the main source of information for decoding.  
690 These are of considerably lower frequency than the primary spatial frequency charac-  
691 teristics of the columnar organization and are lower than the Nyquist criterion of the  
692 BOLD fMRI sampling frequencies.

693 It could be speculated that the spatial scale of the orientation signal as estimated  
694 by volumetric spatial filtering is, to some degree, determined by the representation  
695 of the cortical folding pattern in the scan volume. As volumetric filtering procedures  
696 using 3D Gaussian kernels inherently mixes signals from gray matter, white matter,  
697 and superficial vessels. It might be that a volumetric BP filter corresponding to the  
698 most informative spatial frequency band is beneficial because it is of sufficient size to  
699 average signal across the entire diameter of the folded calcarine sulcus, whereas a smaller  
700 filter is not, and a bigger filter includes a substantial fraction of the surrounding white  
701 matter and adjacent cortical fields. If the above speculation is correct, we could expect  
702 lower decoding accuracy in the most informative band when replacing the employed  
703 spatial filtering procedure with a cortical surface-based smoothing or a spatial filtering  
704 that is restricted to V1 ROIs in each hemisphere. We performed these two alternative  
705 analyses and found only minor differences in the results (see supplementary material  
706 Fig. S3). Similar to the report of Swisher et al. (2010), the band-pass, high-pass, low-  
707 pass components based on these alternative spatial smoothing schemes perform very  
708 similar, but are more evenly sloped with increasing filter size compared to unconstrained  
709 volumetric filtering. Except for the 0.8 mm data, where the insufficient signal is even  
710 more evident, the BP performance is extremely similar. We conclude that there is little  
711 evidence for an impact of standard, unmasked, volumetric spatial filtering for this type  
712 of decoding analysis, compared to alternative procedures.

### 713 *Veins contribute signal usable for orientation decoding*

714 Several studies have cited an orientation-related BOLD signal originating from the  
715 vascular system (draining veins) as a potential information source for decoding that

716 may introduce spatial biases in the representation of orientation as measured with  
717 fMRI (Kriegeskorte et al., 2010; Chaimow et al., 2011; Shmuel et al., 2010). The  
718 present results confirm the availability of such a signal. Particularly for the two highest  
719 resolutions tested here the decoding accuracy obtained from voxels sampling veins is  
720 equal to the performance obtained from the non-venous rest of the V1 ROI, or even  
721 outperforms it when controlling for the number of input voxels for the classification  
722 model (Fig. 6A).

723 A BOLD signal originating in the blood vessels has the potential to introduce com-  
724 plex transformations of the spatial representation of orientation in the BOLD response  
725 patterns. Due to the structural properties of the vascular system this signal is likely  
726 to be of lower spatial frequency, compared to the underlying neuronal activation pat-  
727 tern, and is superimposed on a potential high-frequency pattern reflecting the columnar  
728 structure of V1. This explanation has been put forth by Kriegeskorte et al. (2010) who  
729 describe voxels as “complex spatio-temporal filters” and our results are compatible with  
730 this model. However, gradient echo BOLD fMRI is highly sensitive to large draining  
731 veins (Gardner, 2010; Shmuel et al., 2010; Chaimow et al., 2011), which might influence  
732 the BOLD signal also at a considerable distance from the blood vessel, rendering the  
733 interpretation of these findings even more difficult.

734 It should also be mentioned that previous studies found a substantial reduction of  
735 intra-vascular BOLD signals at higher magnetic field strength (Yacoub et al., 2001),  
736 and enhanced signal contributions from microvascular structures at 7T (Shmuel et al.,  
737 2007). Consequently, the particular composition of the compound signal captured with  
738 BOLD fMRI will vary with the magnetic field strength. A future study should compare  
739 the present results with data acquisitions at a different field strength to shed more light  
740 on nature of the underlying signal and the implications for decoding analysis.

741 *Limitations.* The focus of the present study was to investigate the effect of acquisition  
742 resolution and spatial filtering on the decoding of visual orientations from primary  
743 visual cortex. In order to yield comparable results, the acquisition parameters were  
744 constrained to guarantee a certain minimum coverage of the V1 ROI even at the highest  
745 resolutions and to have an identical temporal sampling frequency (TR) to yield the same  
746 number of observations across all resolutions. This choice implied that the GRAPPA  
747 acceleration factor had to be increased with increasing resolution, hence leading to an  
748 increased under-sampling of the k-space with higher resolutions. This could impact the  
749 sensitivity of the scan to high-frequency spatial signals. A future study will have to test  
750 whether the present findings hold when constraints on coverage and sampling frequency  
751 are relaxed. For example, a study by De Martino et al. (2013) using a 3D gradient and  
752 spin echo (GRASE) sequence suggests that such a sequence outperforms a gradient  
753 echo sequence, such as the one employed in this study, for high-resolution imaging at  
754 0.8 mm isotropic resolution — at the expense of a vastly reduced scan volume.

755 The present study is exclusively based on 7 Tesla fMRI data, hence it remains unclear  
756 in which way the characteristics of the relation of decoding performance and acquisition  
757 resolution are dependent on MR field-strength. The differences in the sizes of the BOLD  
758 point-spread functions (Shmuel et al., 2007; Engel et al., 1997) suggest a lower resolution  
759 limit for 3 Tesla scans. However, the reported optimal resolution is within the range of  
760 conventional acquisition resolutions of today’s 3 Tesla scanners. A future study should

761 address the question of how the decoding performance varies with field-strength for  
762 identical resolutions.

763 While this study focused on the optimal acquisition parameters for decoding of  
764 visual orientation from fMRI BOLD response patterns in early visual cortex, we ac-  
765 knowledge other possibilities of further optimization of the decoding procedure (clas-  
766 sification algorithm, hyper-parameter optimization, etc.) and their potential impacts  
767 on results and interpretations. To facilitate the required future analyses we have pub-  
768 licly released the data (available without restrictions from GitHub <https://github.com/psychoinformatics-de/studyforrest-data-multires7t>) and a “Data in brief”  
769 manuscript along with this. In this study we have found that given a neural signal with  
770 known fine-scale spatial characteristics, there are technical and physiological factors  
771 that place the acquisition resolution optimal for decoding at a substantially coarser  
772 scale. Future studies should investigate whether the optimal settings for other decod-  
773 ing paradigms and different cortical areas, beyond the findings for visual orientation  
774 in visual cortex presented here, and the congruent results for auditory representations  
775 reported by Gardumi et al. (2016), are similar in nature.  
776

### 777 *Acknowledgements*

778 We thank Yukiyasu Kamitani, as well as Nikolaus Kriegeskorte and two additional  
779 anonymous reviewers their critical feedback on this research, Florian Baumgartner for  
780 his advice on data analysis, and Alex Waite for his tireless support of the computational  
781 infrastructure required for this research, and for his feedback regarding the language of  
782 this manuscript. This research was supported by a grant from the German Research  
783 Foundation (DFG) awarded to S. Pollmann and O. Speck (DFG PO 548/15-1). This  
784 research was, in part, also supported by the German Federal Ministry of Education and  
785 Research (BMBF) as part of a US-German collaboration in computational neuroscience  
786 (CRCNS; awarded to J. V. Haxby, P. Ramadge, and M. Hanke), co-funded by the  
787 BMBF and the US National Science Foundation (BMBF 01GQ1112; NSF 1129855).  
788 M. Hanke was supported by funds from the German federal state of Saxony-Anhalt  
789 and the European Regional Development Fund (ERDF), project: Center for Behavioral  
790 Brain Sciences.

### 791 *Conflict of interest*

792 The authors declare no competing interest.

## 793 **References**

- 794 Adams, D.L., Sincich, L.C., Horton, J.C., 2007. Complete pattern of ocular dominance  
795 columns in human primary visual cortex. *The Journal of Neuroscience* 27, 10391–  
796 10403.
- 797 Alink, A., Krugliak, A., Walther, A., Kriegeskorte, N., 2013. fMRI orientation decoding  
798 in V1 does not require global maps or globally coherent orientation stimuli. *Front*  
799 *Psychol* 4, 493. doi:10.3389/fpsyg.2013.00493.
- 800 Op de Beeck, H., 2010. Probing the mysterious underpinnings of multi-voxel fMRI  
801 analyses. *Neuroimage* 50, 567–71. doi:10.1016/j.neuroimage.2009.12.072.

- 802 Bellman, R.E., 1961. Adaptive control processes: a guided tour. volume 4. Princeton  
803 University Press: Princeton.
- 804 Bonte, M., Hausfeld, L., Scharke, W., Valente, G., Formisano, E., 2014. Task-dependent  
805 decoding of speaker and vowel identity from auditory cortical response patterns. *The*  
806 *Journal of Neuroscience* 34, 4548–4557.
- 807 Carlson, T.A., 2014. Orientation decoding in human visual cortex: new insights from  
808 an unbiased perspective. *The Journal of Neuroscience* 34, 8373–8383. doi:10.1523/  
809 JNEUROSCI.0548-14.2014.
- 810 Chaimow, D., Yacoub, E., Ugurbil, K., Shmuel, A., 2011. Modeling and analysis  
811 of mechanisms underlying fMRI-based decoding of information conveyed in cortical  
812 columns. *Neuroimage* 56, 627–42. doi:10.1016/j.neuroimage.2010.09.037.
- 813 Chang, C.C., Lin, C.J., 2011. LIBSVM: A library for support vector machines. *ACM*  
814 *Transactions on Intelligent Systems and Technology* 2, 27:1–27:27. doi:10.1145/  
815 1961189.1961199. Software available at [http://www.csie.ntu.edu.tw/~cjlin/  
816 libsvm](http://www.csie.ntu.edu.tw/~cjlin/libsvm/).
- 817 Cox, R.W., 1996. AFNI: software for analysis and visualization of functional magnetic  
818 resonance neuroimages. *Computers and Biomedical research* 29, 162–173. doi:10.  
819 1006/cbmr.1996.0014.
- 820 Dale, A.M., Fischl, B., Sereno, M.I., 1999. Cortical surface-based analysis: I. Segmen-  
821 tation and surface reconstruction. *Neuroimage* 9, 179–194. doi:10.1006/nimg.1998.  
822 0395.
- 823 De Martino, F., Zimmermann, J., Muckli, L., Ugurbil, K., Yacoub, E., Goebel, R., 2013.  
824 Cortical depth dependent functional responses in humans at 7t: improved specificity  
825 with 3d grase. *PloS one* 8, e60514. doi:10.1371/journal.pone.0060514.
- 826 Dou, W., Speck, O., Benner, T., Kaufmann, J., Li, M., Zhong, K., Walter, M., 2014. Au-  
827 tomatic voxel positioning for MRS at 7 t. *Magnetic Resonance Materials in Physics,*  
828 *Biology and Medicine* 28, 259–270. doi:10.1007/s10334-014-0469-9.
- 829 Edwards, A.L., 1948. Note on the “correction for continuity” in testing the significance  
830 of the difference between correlated proportions. *Psychometrika* 13, 185–187.
- 831 Engel, S.A., Glover, G.H., Wandell, B.A., 1997. Retinotopic organization in human  
832 visual cortex and the spatial precision of functional MRI. *Cerebral cortex* 7, 181–  
833 192. doi:10.1093/cercor/7.2.181.
- 834 Freeman, J., Brouwer, G., Heeger, D., Merriam, E., 2011. Orientation decoding depends  
835 on maps, not columns. *J Neurosci* 31, 4792–804. doi:10.1523/JNEUROSCI.5160-10.  
836 2011.
- 837 Freeman, J., Heeger, D., Merriam, E., 2013. Coarse-scale biases for spirals and orien-  
838 tation in human visual cortex. *J Neurosci* 33, 19695–703. doi:10.1523/JNEUROSCI.  
839 0889-13.2013.

- 840 Friedman, J., Hastie, T., Tibshirani, R., 2001. The elements of statistical learning.  
841 volume 1. Springer series in statistics Springer, Berlin.
- 842 Furmanski, C.S., Engel, S.A., 2000. An oblique effect in human primary visual cortex.  
843 Nature Neuroscience 3, 535–536. doi:10.1038/75702.
- 844 Gardner, J.L., 2010. Is cortical vasculature functionally organized? NeuroImage 49,  
845 1953–1956. doi:10.1016/j.neuroimage.2009.07.004.
- 846 Gardumi, A., Ivanov, D., Hausfeld, L., Valente, G., Formisano, E., Uludağ, K., 2016.  
847 The effect of spatial resolution on decoding accuracy in fmri multivariate pattern  
848 analysis. NeuroImage 132, 32–42.
- 849 Glover, G.H., 1999. Deconvolution of impulse response in event-related BOLD fMRI.  
850 Neuroimage 9, 416–429. doi:10.1006/nimg.1998.0419.
- 851 Haacke, E.M., Xu, Y., Cheng, Y.C.N., Reichenbach, J.R., 2004. Susceptibility weighted  
852 imaging (swi). Magnetic Resonance in Medicine 52, 612–618. doi:10.1002/mrm.  
853 20198.
- 854 Halchenko, Y.O., Hanke, M., 2012. Open is not enough. Let’s take the next step: An  
855 integrated, community-driven computing platform for neuroscience. Front. Neuroin-  
856 form. 6. doi:10.3389/fninf.2012.00022.
- 857 Hanke, M., Baumgartner, F.J., Ibe, P., Kaule, F.R., Pollmann, S., Speck, O., Zinke,  
858 W., Stadler, J., 2014. A high-resolution 7-Tesla fMRI dataset from complex natural  
859 stimulation with an audio movie. Scientific Data 1. doi:10.1038/sdata.2014.3.
- 860 Hanke, M., Halchenko, Y., Sederberg, P., Olivetti, E., Fründ, I., Rieger, J., Herrmann,  
861 C., Haxby, J., Hanson, S., Pollmann, S., 2009. PyMVPA: A Unifying Approach to  
862 the Analysis of Neuroscientific Data. Front Neuroinform 3, 3. doi:10.3389/neuro.  
863 11.003.2009.
- 864 Haxby, J.V., 2012. Multivariate pattern analysis of fMRI: the early beginnings. Neu-  
865 roimage 62, 852–855. doi:10.1016/j.neuroimage.2012.03.016.
- 866 Haynes, J., Rees, G., 2005. Predicting the orientation of invisible stimuli from activity  
867 in human primary visual cortex. Nat Neurosci 8, 686–91. doi:10.1038/nn1445.
- 868 Haynes, J.D., 2009. Decoding visual consciousness from human brain signals. Trends  
869 in cognitive sciences 13, 194–202.
- 870 Heidemann, R.M., Ivanov, D., Trampel, R., Fasano, F., Meyer, H., Pfeuffer, J., Turner,  
871 R., 2012. Isotropic submillimeter fMRI in the human brain at 7T: Combining re-  
872 duced field-of-view imaging and partially parallel acquisitions. Magnetic Resonance  
873 in Medicine 68, 1506–1516. doi:10.1002/mrm.24156.
- 874 In, M.H., Speck, O., 2012. Highly accelerated PSF-mapping for EPI distortion correc-  
875 tion with improved fidelity. Magnetic Resonance Materials in Physics, Biology and  
876 Medicine 25, 183–192.

- 877 Jenkinson, M., 2003. Fast, automated, N-dimensional phase-unwrapping algorithm.  
878 *Magnetic resonance in medicine* 49, 193–197. doi:10.1002/mrm.10354.
- 879 Jones, E., Oliphant, T., Peterson, P., et al., 2001. SciPy: Open source scientific tools  
880 for Python. URL: <http://www.scipy.org/>. [Online; accessed 2015-07-28].
- 881 Kamitani, Y., Sawahata, Y., 2010. Spatial smoothing hurts localization but not in-  
882 formation: pitfalls for brain mappers. *Neuroimage* 49, 1949–52. doi:10.1016/j.  
883 *neuroimage*.2009.06.040.
- 884 Kamitani, Y., Tong, F., 2005. Decoding the visual and subjective contents of the human  
885 brain. *Nat Neurosci* 8, 679–85. doi:10.1038/nn1444.
- 886 Kriegeskorte, N., Bandettini, P., 2007. Analyzing for information, not activation, to  
887 exploit high-resolution fMRI. *Neuroimage* 38, 649–62. doi:10.1016/j.*neuroimage*.  
888 2007.02.022.
- 889 Kriegeskorte, N., Cusack, R., Bandettini, P., 2010. How does an fMRI voxel sam-  
890 ple the neuronal activity pattern: compact-kernel or complex spatiotemporal filter?  
891 *Neuroimage* 49, 1965–76. doi:10.1016/j.*neuroimage*.2009.09.059.
- 892 Millman, K.J., Brett, M., 2007. Analysis of functional magnetic resonance imaging in  
893 Python. *Computing in Science & Engineering* 9, 52–55. doi:10.1109/MCSE.2007.46.
- 894 Misaki, M., Luh, W., Bandettini, P., 2013. The effect of spatial smoothing on fMRI de-  
895 coding of columnar-level organization with linear support vector machine. *J Neurosci*  
896 *Methods* 212, 355–61. doi:10.1016/j.*jneumeth*.2012.11.004.
- 897 Obermayer, K., Blasdel, G.G., 1993. Geometry of orientation and ocular dominance  
898 columns in monkey striate cortex. *The Journal of Neuroscience* 13, 4114–4129.
- 899 Pedregosa, F., Varoquaux, G., Gramfort, A., Michel, V., Thirion, B., Grisel, O., Blon-  
900 del, M., Prettenhofer, P., Weiss, R., Dubourg, V., et al., 2011. Scikit-learn: Machine  
901 learning in Python. *The Journal of Machine Learning Research* 12, 2825–2830.
- 902 Peirce, J.W., 2008. Generating stimuli for neuroscience using PsychoPy. *Frontiers in*  
903 *neuroinformatics* 2. doi:10.3389/*neuro*.11.010.2008.
- 904 Pereira, F., Mitchell, T., Botvinick, M., 2009. Machine learning classifiers and fMRI:  
905 a tutorial overview. *Neuroimage* 45, S199–S209. doi:10.1016/j.*neuroimage*.2008.  
906 11.007.
- 907 Sengupta, A., Kaule, F., Guntupalli, J.S., HHoffmann, M., Häusler, C., Stadler, J.,  
908 Hanke, M., 2016. An extension of the studyforrest dataset for vision research. *Scien-*  
909 *tific Data* , Under review URL: [http://biorxiv.org/content/early/2016/03/31/](http://biorxiv.org/content/early/2016/03/31/046573)  
910 046573.
- 911 Shmuel, A., Chaimow, D., Raddatz, G., Ugurbil, K., Yacoub, E., 2010. Mechanisms  
912 underlying decoding at 7T: ocular dominance columns, broad structures, and macro-  
913 scopic blood vessels in V1 convey information on the stimulated eye. *Neuroimage* 49,  
914 1957–1964. doi:10.1016/j.*neuroimage*.2009.08.040.

- 915 Shmuel, A., Yacoub, E., Chaimow, D., Logothetis, N., Ugurbil, K., 2007. Spatio-  
916 temporal point-spread function of fMRI signal in human gray matter at 7 Tesla.  
917 *Neuroimage* 35, 539–52. doi:10.1016/j.neuroimage.2006.12.030.
- 918 Smith, S., Jenkinson, M., Woolrich, M., Beckmann, C., Behrens, T., Johansen-Berg, H.,  
919 Bannister, P., De, L.M., Drobnjak, I., Flitney, D., Niazy, R., Saunders, J., Vickers,  
920 J., Zhang, Y., De, S.N., Brady, J., Matthews, P., 2004. Advances in functional and  
921 structural MR image analysis and implementation as FSL. *Neuroimage* 23 Suppl 1,  
922 S208–19. doi:10.1016/j.neuroimage.2004.07.051.
- 923 Swisher, J., Gatenby, J., Gore, J., Wolfe, B., Moon, C., Kim, S., Tong, F., 2010. Mul-  
924 tiscale pattern analysis of orientation-selective activity in the primary visual cortex.  
925 *J Neurosci* 30, 325–30. doi:10.1523/JNEUROSCI.4811-09.2010.
- 926 Tong, F., Harrison, S., Dewey, J., Kamitani, Y., 2012. Relationship between BOLD  
927 amplitude and pattern classification of orientation-selective activity in the human  
928 visual cortex. *Neuroimage* 63, 1212–22. doi:10.1016/j.neuroimage.2012.08.005.
- 929 Triantafyllou, C., Hoge, R., Krueger, G., Wiggins, C., Potthast, A., Wiggins, G., Wald,  
930 L., 2005. Comparison of physiological noise at 1.5 T 3 T and 7 T and optimization of  
931 fMRI acquisition parameters. *NeuroImage* 26, 243–250. doi:10.1016/j.neuroimage.  
932 2005.01.007.
- 933 Ugurbil, K., 2012. The road to functional imaging and ultrahigh fields. *Neuroimage*  
934 62, 726–35. doi:10.1016/j.neuroimage.2012.01.134.
- 935 Warnking, J., Dojat, M., Guérin-Dugué, A., Delon-Martin, C., Olympieff, S., Richard,  
936 N., Chéhikian, A., Segebarth, C., 2002. fMRI retinotopic mapping—step by step.  
937 *Neuroimage* 17, 1665–83. doi:10.1006/nimg.2002.1304.
- 938 Weibull, A., Gustavsson, H., Mattsson, S., Svensson, J., 2008. Investigation of spatial  
939 resolution, partial volume effects and smoothing in functional MRI using artificial  
940 3d time series. *NeuroImage* 41, 346–353. URL: [http://dx.doi.org/10.1016/j.](http://dx.doi.org/10.1016/j.neuroimage.2008.02.015)  
941 [neuroimage.2008.02.015](http://dx.doi.org/10.1016/j.neuroimage.2008.02.015), doi:10.1016/j.neuroimage.2008.02.015.
- 942 Yacoub, E., Harel, N., Ugurbil, K., 2008. High-field fMRI unveils orientation columns in  
943 humans. *Proc Natl Acad Sci U S A* 105, 10607–12. doi:10.1073/pnas.0804110105.
- 944 Yacoub, E., Shmuel, A., Pfeuffer, J., De Moortele, V., Adriany, G., Andersen, P.,  
945 Vaughan, J.T., Merkle, H., Ugurbil, K., Hu, X., et al., 2001. Imaging brain function  
946 in humans at 7 tesla. *Magnetic Resonance in Medicine* 45, 588–594.
- 947 Zhang, F., Wang, J.P., Kim, J., Parrish, T., Wong, P.C., 2015. Decoding multiple  
948 sound categories in the human temporal cortex using high resolution fmri. *PloS one*  
949 10, e0117303.

## Supplementary materials and methods

950

### *Experimental Design*

951

952 This section describes how the display sequence of the oriented gratings in both the  
953 hemifields were generated per experimental run. Independent sequences were gener-  
954 ated per hemifield with equal number of occurrences of each orientation. There were  
955 4 different orientations ( $0^\circ$ ,  $45^\circ$ ,  $90^\circ$ , or  $135^\circ$ ) each occurring for 5 times in the se-  
956 quence, contributing to 20 trials in one run. The sequences were randomly shuffled  
957 per hemifield. In this analysis a single GLM was used to model the events in both the  
958 hemifields. This was done to account for potential inter-hemispheric cross-talk due to  
959 the simultaneous bilateral stimulation, and correlation in this stimulus sequence be-  
960 tween hemifields. Moreover, in order to minimize undesired attention shift effects, we  
961 opted for a simultaneous onsets of the stimulation in both hemifields. Combined with  
962 the further constraint of the same number of stimulation trials per orientation in both  
963 hemifields, this would unavoidably lead to a singularity of the GLM design matrix,  
964 unless a further source of temporal variability is introduced. In order to address this  
965 issue unilateral stimulation events (termed NULL events) were introduced and included  
966 in the GLM.

967 For comparison, we additionally analyzed these data using two separate models for  
968 both hemifields, while excluding NULL events from the modeling. This resulted in an  
969 overall improved classification performance, but did not impact the structure of the  
970 relative performance differences between resolutions (0.8 mm: 32.32%, 1.4 mm:41.78%,  
971 2.0 mm: 46.42%, and 3.0 mm: 40.17%) Figure S1 illustrates the combined impact of  
972 potential interhemispheric cross-talk and random correlations of the stimulus sequence  
973 between hemispheres by comparing the decoding performance in the contralateral and  
974 ipsilateral V1 ROI.

### *Alternative spatial filtering procedures*

975

976 In Figure 4 the performance of orientation decoding was quantified following low-  
977 pass, high-pass, band-pass, and band-stop spatial filtering in order to study the spatial  
978 frequency dependent orientation selective responses. All spatial filtering procedures  
979 were volumetric, using 3D Gaussian kernels and ROI voxel selection was performed after  
980 spatial filtering with different Gaussian kernel widths on the entire volume. Though  
981 this 3D filtering procedure was being extensively used in previous studies like (Op de  
982 Beeck, 2010; Swisher et al., 2010), this approach leads to information propagation  
983 from adjacent parts of the cortex, white matter and superficial vessels. Moreover,  
984 unconstrained 3D filtering does not respect the cortical folding pattern and, given a  
985 large enough filter, can smooth across sulcal boundaries, such as the two banks of the  
986 calcarine sulcus. This confounds filter width with the extent of the cortical region from  
987 which information is drawn. To avoid this problem, two additional spatial filtering  
988 approaches were implemented, namely volumetric filtering restricted to the V1 ROI,  
989 and surface-based smoothing.

990 *Volumetric filtering restricted to the V1 ROI.* Similar to the spatial filtering procedure  
991 performed in Alink et al. (2013), the voxel values outside the V1 ROI were considered  
992 to be missing values (NaN) instead of applying spatial filtering on the whole volume,

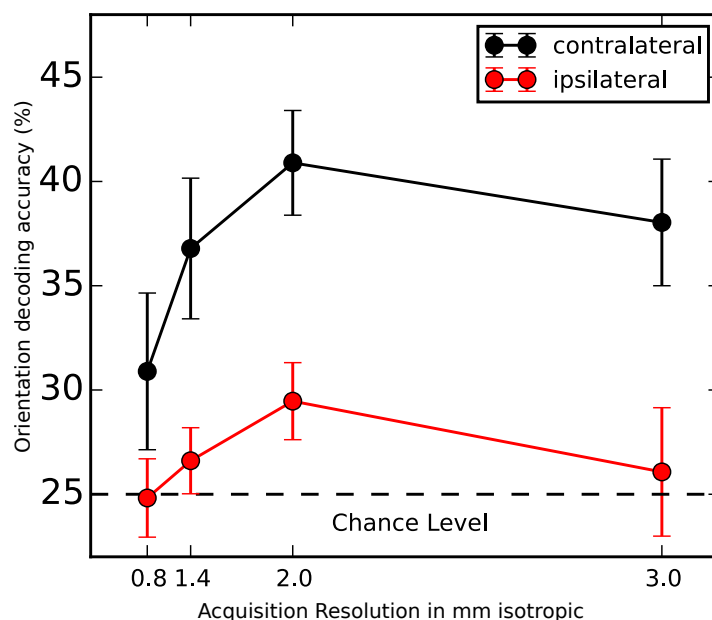


Figure S1: Orientation decoding accuracy on spatially unfiltered data across acquisition resolutions in both contralateral and ipsilateral V1 ROI. The ipsilateral accuracies show similar trend as the contralateral accuracies. The ipsilateral accuracies for 1.4 mm and 2 mm resolution show low decoding performance and the 0.8 mm and 3 mm decoding accuracies are at chance level.

993 prior to any masking. To eliminate a potential effect of smoothing across hemispheres  
994 with large Gaussian kernels, filtering was restricted to individual hemispheres. First,  
995 voxel values outside the left V1 ROI was considered to be NaNs and spatial smoothing  
996 was applied. The same procedure was applied to the right ROI, and then the smoothed  
997 left and right V1 ROI were combined to form the smoothed BOLD volume. The same  
998 nested cross validation approach was performed on the smoothed data. The results  
999 of this analysis are highly similar to the results for the unconstrained filtering prior  
1000 masking (Fig. S3 A-D).

1001 *Surface-based smoothing.* Freesurfer's `mri_vol2surf` function (Dale et al., 1999) was  
1002 used for smoothing gray matter BOLD data on the cortical surface, while specifying  
1003 the filter size with the `surf-fwhm` parameter. In the next step surface-projected data  
1004 were mapped back into the BOLD volume using Freesurfer's `mri_surf2vol` function  
1005 (tri-linear interpolation, `fill-projfrac` parameter with range 0-1 in steps of 0.01).  
1006 This procedure was performed for each hemisphere separately. Back projection into  
1007 the volume was performed to maintain an equal number of input features for the de-  
1008 coding analysis. To illustrate the effect of surface based filtering, Figure S2 shows the  
1009 reconstructed surface of one participant, with the average modeled response to cardinal  
1010 and oblique orientations, filtered with 3 different filter FWHMs.

1011 Subsequently, the same nested cross validation approach was performed on the  
1012 smoothed data. The results of this analysis are shown in Figure S3 E-H. The re-  
1013 sults of surface based smoothing were similar to those of the 3D Gaussian filter, but  
1014 the decoding accuracy did not decrease as rapidly with larger kernels. The band pass  
1015 filtering peak was present at  $\approx 5-8$  mm but less pronounced and more evenly sloped than  
1016 what was obtained from volumetric filtering.

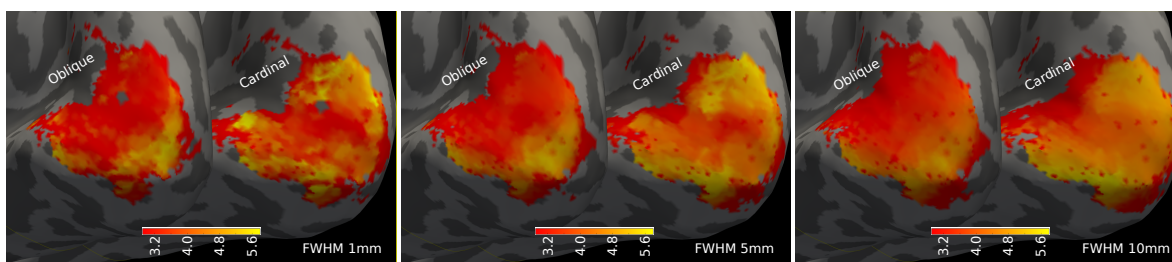


Figure S2: Surface-rendering of BOLD response patterns for one participant (2 mm acquisition, sub-21), after surface-based smoothing with three kernel sizes. Overlays indicate the modeled average response to cardinal and oblique orientations ( $Z$ -score) in the manually delineated V1 region, thresholded at  $p < 0.05$  (voxelwise).

1017 *Resampling procedure to other resolutions*

1018 Resampling BOLD fMRI data from one resolution to the other was implemented  
1019 as a two-step procedure. In the following, we describe the procedure using resampling  
1020 from 0.8 mm to 3.0 mm resolution as an example, but the procedure was analogous for  
1021 all resolution pairs.

1022 First FFT-based spatial filtering was performed on the distortion corrected 0.8 mm  
1023 data (see Figure S4A) using the `scipy` function `signal.resample()`. This removed  
1024 the higher frequency components, but the voxel grid remained unchanged (in-plane  
1025 matrix size (208, 160) with 32 slices). In the next step, linear resampling/reslicing was  
1026 performed with `nilearn` function `resample_img()` to convert the FFT filtered image  
1027 to the corresponding 3.0 mm voxel grid (see Fig. S4B for an example). Importantly,  
1028 other than changing the voxel size, no further transformation, for example, to align  
1029 a resampled image to the orientation of the corresponding native acquisition, were  
1030 applied.

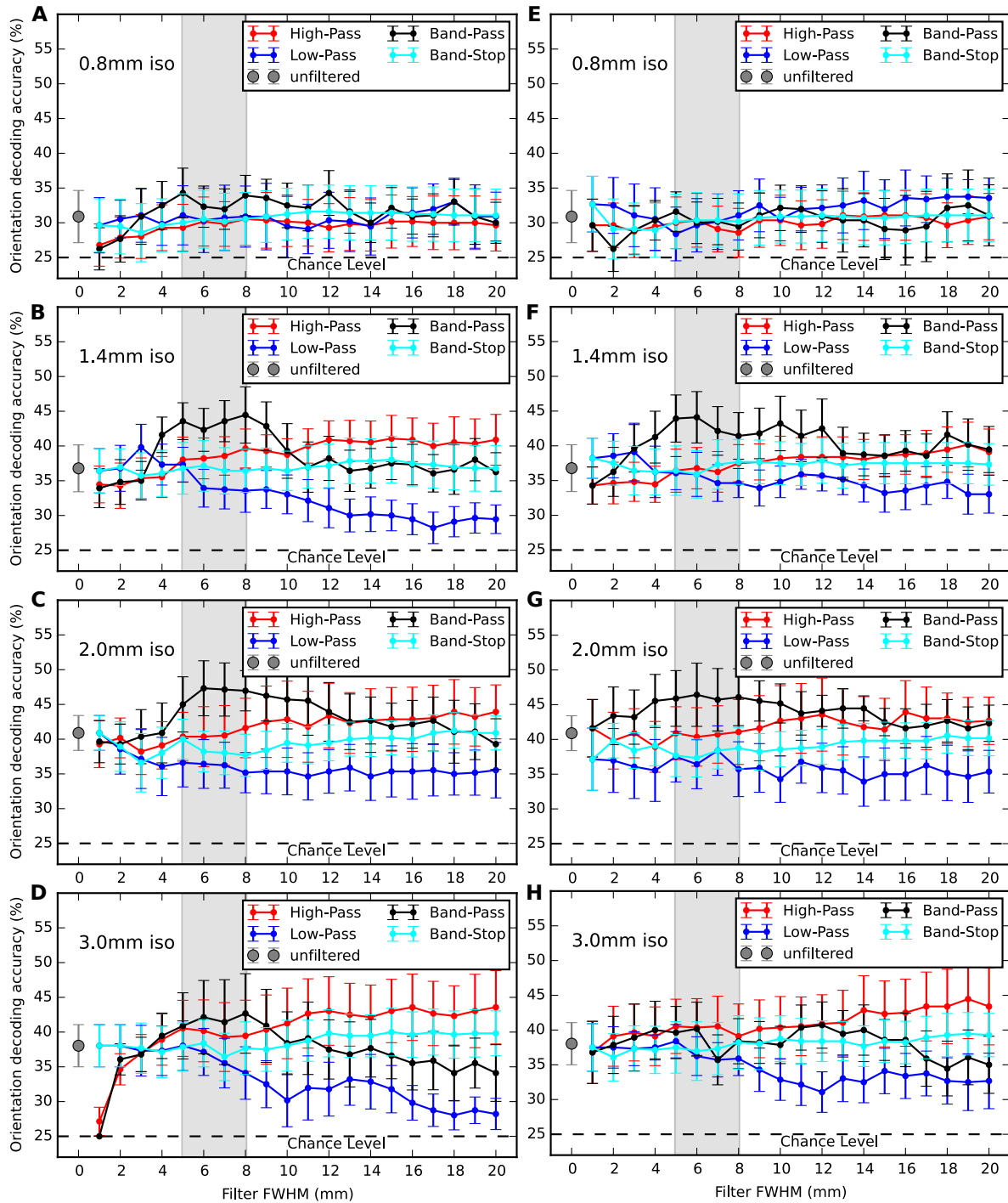


Figure S3: Results of alternative spatial filtering procedures (analog to Fig. 4). Volumetric spatial filtering restricted to V1 ROI (A-D), cortical surface-based smoothing (E-H).

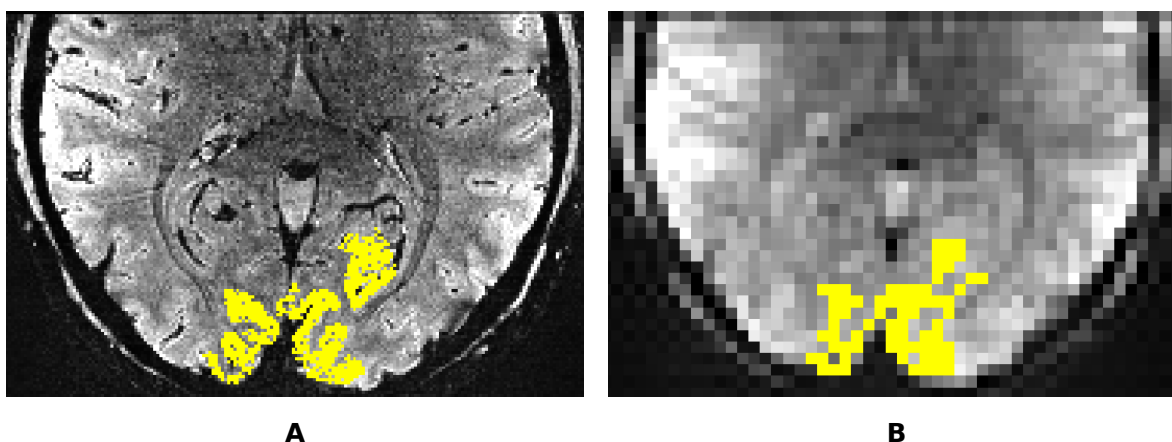


Figure S4: Illustration of resampling from 0.8 mm to 3.0 mm resolution. (A) Distortion corrected 0.8mm isotropic BOLD image with superimposed V1 ROI mask. (B) After removal of high-frequency components using scipy function `signal.resample()` superimposed with resampled V1 ROI mask (linear interpolation using scipy function `ndimage.interpolation.zoom()`)

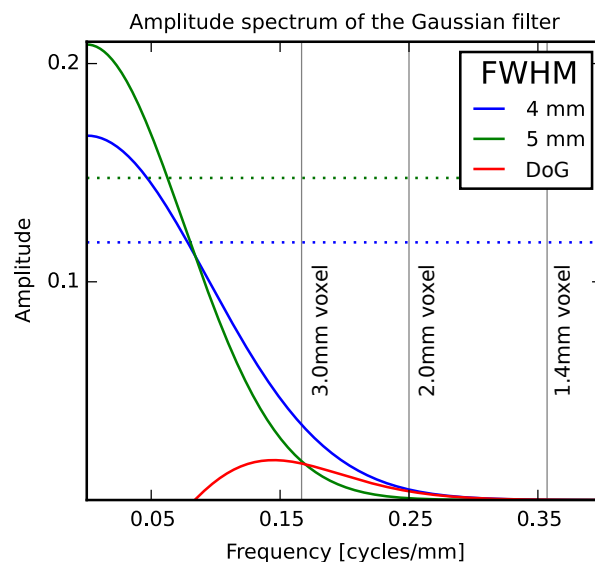


Figure S5: Illustration of the attenuation profile of a Difference-of-Gaussian (DoG) band-pass filter. The blue and green curve represent the profiles of Gaussian low-pass filters (4 mm and 5 mm respectively) in the frequency domain. Horizontal lines represent the -3 db points of the Gaussians. Band-pass filtering is implemented by subtracting the two low-pass filter outputs from each other. The profile of the resulting DoG band-pass filter is shown in red. Vertical lines show the Nyquist-frequencies for the three lowest resolutions in the study. The pass-band of this exemplary DoG filter (corresponding to an axis label "5 mm" in Figure 4 contains frequencies higher than what can be adequately measured with a 3 mm acquisition.

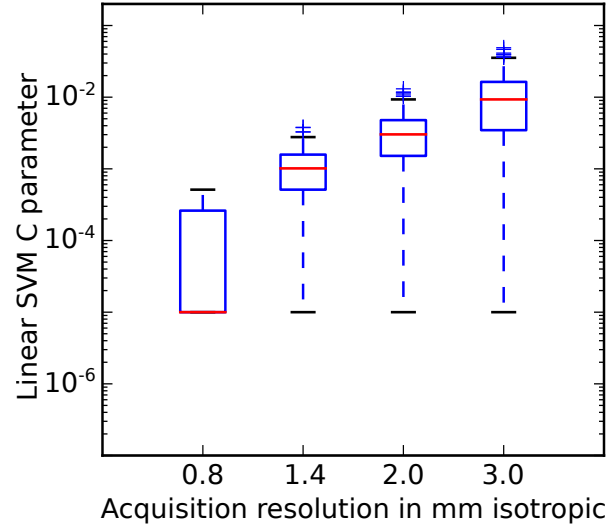


Figure S6: Range of tuned Linear SVM C parameters in the orientation decoding analysis across different resolutions.

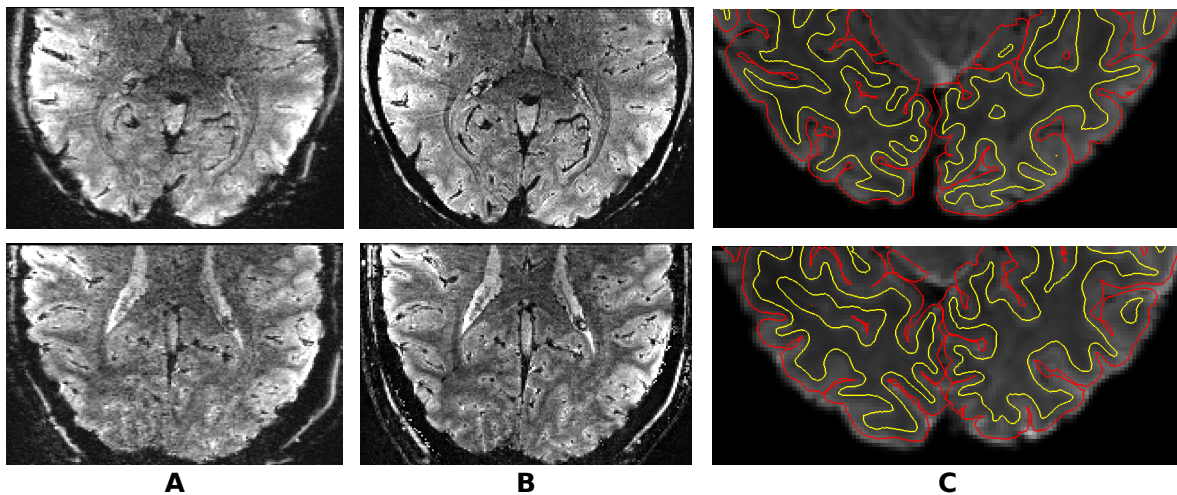


Figure S7: Illustration of the alignment of distortion corrected BOLD images obtained at 7 Tesla to the structural data obtained at 3 Tesla for 2 subjects. (A) Uncorrected image from Siemens 7T Magnetom (B) Distortion-corrected image (In and Speck, 2012) (C) Alignment of the BOLD image and the cortical surface, reconstructed from the corresponding structural scans. The white matter segmentation is shown in yellow and the pial surface in red.

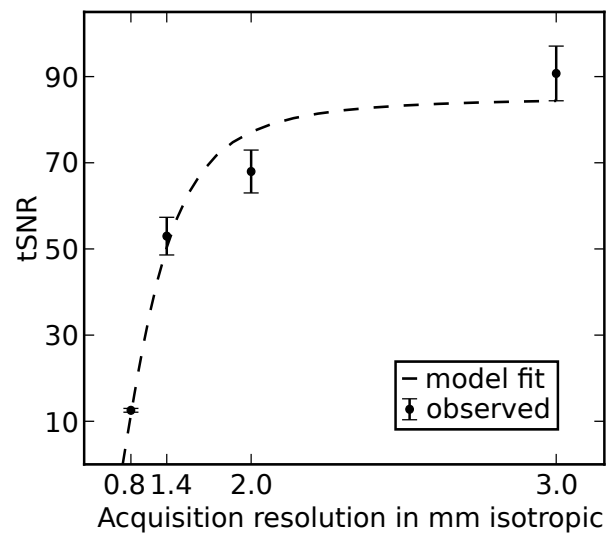


Figure S8: Temporal signal-to-noise ratio (tSNR) as a function of voxel volume. The observed data are represented by dots and the error bars represent the SEM across subjects. The dashed line shows the fit to the following model  $tSNR = \kappa V / \sqrt{1 + \lambda^2 \kappa^2 V^2}$  similar to the report of Triantafyllou et al. (2005)